

Fire-Atmosphere Interactions in the Wildland-Urban Interface Using High-Fidelity Experimental Simulations

Dongqi Lin^{1*}, Marwan Katurji¹, Peyman Zawar-Reza¹, Alena Malyarenko^{1,2},
Andres Valencia³, Jiawei Zhang⁴

¹Te Kura Aronukurangi / School of Earth and Environment, Te Whare Wānanga o Waitaha / University of Canterbury, Ōtautahi / Christchurch, Aotearoa / New Zealand

²Te Puna Pātīotio / Antarctic Research Centre, Te Herenga-Waka / Victoria University of Wellington, Aotearoa / New Zealand

³Te Tari Pūhanga Metarahi, Rawa Taiao / Department of Civil and Natural Resources Engineering, Te Whare Wānanga o Waitaha / University of Canterbury, Ōtautahi / Christchurch, Aotearoa / New Zealand

⁴New Zealand Forest Research Institute, Scion, Ōtautahi / Christchurch, Aotearoa / New Zealand

Key Points:

- Wildland-urban interface
- Fire-atmosphere interactions

*Now at ARC Centre of Excellence for Climate Extremes, Monash University, Melbourne, Australia

Corresponding author: Dongqi Lin, dongqi.lin@monash.edu

Abstract

With increased urbanisation, fires in the wildland urban interface (WUI) have become a severe problem worldwide. The unique features of WUI may influence fire-atmosphere interactions. This study utilises the parallelized large eddy simulation model (PALM) system for fire-atmosphere simulations of Bottle Lake Forest, Christchurch, New Zealand. Over 3000 residential buildings are situated around the 7 km² forest, with many homes only 50 m away from the forest edge. We conducted high-fidelity fire-atmosphere simulations with the finest grid spacing of 4 m. In comparison to WUI simulations, flat terrain simulations were carried out as a reference for idealised scenarios. Fire-weather conditions for the 2022/2023 New Zealand fire season were selected based on the Fire Weather Index (FWI). Data from previous fire field campaigns were obtained to represent the fire heat forcing. Our results show that the WUI simulation coincides with fire heat transport going further downwind than its flat terrain counterpart. Kelvin-Helmholtz waves were present in both the WUI and flat terrain simulations, generating downdrafts from higher levels to the surface. However, downwind heat transport coincides with a pulsing behavior only in the WUI. In addition to these characteristics, analysis of the ambient atmosphere shows that the WUI plays the main role in modifying fire-atmosphere interactions. This study is the first to simulate fire-atmosphere interactions in WUI with such a high fidelity. Our results provide insights into the impact of WUI on fire-atmosphere dynamics. More work is needed to further understand how each component of WUI can alter fire-atmosphere interactions.

Plain Language Summary

The wildland-urban interface (WUI) has its unique environment, and the fire risk in WUIs is increasing. We conducted very high resolutions simulations to understand how important WUI is in fire-atmosphere interactions. A high fire danger day was selected. The location we simulated is the Bottle Lake Forest, Christchurch, New Zealand, where many homes could be burnt if there is a forest fire. The simulations show that fire heat was transported further away from the fire when we included the WUI. We showed how winds differ with and without the WUI. Although Kelvin-Helmholtz waves were present in the ambient atmosphere, the results illustrate that the WUI is the main reason why the fire heat can be transported further along the wind. Our WUI fire simulations demonstrate high fidelity, which has not been previously achieved in other studies. Our results contribute to a better understanding of fire-atmospheric dynamics in the WUI. Further work is still required to better understand how WUI impacts fire-atmosphere interactions in detail.

1 Introduction

The intensity and impacts of wildfires have been growing across the world. From the Arctic to the Amazon, North America to Asia, and Europe to Australia, human settlements have suffered significantly due to wildfires, especially in the wildland-urban interface (WUI) (A. Sullivan et al., 2022). The WUI is usually defined as the area where human development, such as houses, comes into close contact with natural, undeveloped areas dominated by wildland vegetation (Radeloff et al., 2005). The WUI fire problem is usually two-fold, encompassing climate and human activities. Climate is the primary driver of fire activity (Andela et al., 2017). Many studies have found that natural processes are linked to increased wildfire intensity, such as a decrease in fire season precipitation (Holden et al., 2018), and an increase in temperatures (e.g. Gutierrez et al., 2021; Mueller et al., 2020). A drier and warmer climate could lead to longer, hotter, and drier fire seasons, coinciding with more intense fire events and higher mortality. The secondary driver is human activities associated with land-use changes. The expansion of human settlements changes the landscape of the natural wildland. The road development allows easier access to combustible fuels, and the expansion of electrical transmission lines adds more fire risks to the WUI (Chen et al., 2024).

Therefore, the WUI fire problem and its high social and economic costs have become a rising threat.

Similar to countries like the United States, Canada, and Australia, New Zealand witnessed a considerable increase in the total WUI area (Chen et al., 2024). Although New Zealand has a population of only 5 million and covers a land area of approximately 268,021 square kilometers, it has experienced a great number of wildfires in recent years. For the year between 1 July 2020 and 27 June 2021, 4,586 fires occurred, with 13,348 hectares burnt (Fire Emergency New Zealand, 2021). It should be noted that wildfires in New Zealand were relatively rare before the establishment of human settlement in the late 13th century (Perry et al., 2014). Although most of the fires in New Zealand are small (averaging less than 1 hectare; Pearce, 2018), a few large devastating wildfires have occurred during the past few years. In 2017, the Port Hills wildfire burned 1,660 hectares, forced over 1400 residents to evacuate, destroyed 9 homes, and cost millions to suppress, plus much more paid out by the insurers (Pearce, 2018, and citations therein). In 2020, the Lake Ōhau fire burned approximately 5043 hectares and destroyed 48 homes and buildings (Fire Emergency New Zealand, 2022). In 2024, close to the location of the 2017 wildfire, another fire occurred in the Port Hills, causing thousands of people to leave their homes. The exact damage and cause of the 2024 Port Hills fire are still under investigation. Among the many WUIs in New Zealand, in this study, we focus on the WUI of Bottle Lake Forest (BLF), Christchurch, New Zealand. Since Christchurch is the largest city in the South Island of New Zealand, there is a rising concern around its WUI fire problem. Figure 1 shows the location and landscape of the BLF WUI. The BLF area contains a pine forest of over 7 km² surrounded by more than 3000 residential buildings. The pine forest height is approximately 22 m. Many buildings are within 100 m of the forest precinct, which could be under serious fire danger in case of a forest fire in the area.

Various processes and drivers are involved in the WUI fire problem. Here, we focus on the fire-atmosphere interactions and dynamics. The atmospheric and fire processes are multiscale and nonlinear, making fire-atmospheric interactions complex. The atmospheric processes can impact fire from the microscale (sub-meter to kilometer) to the mesoscale (10 to 200 km), while fire modifies the atmospheric flows with its strong forcing of heat (e.g. Dickinson et al., 2021; Finney et al., 2015; A. L. Sullivan, 2017; Zhang et al., 2023). Furthermore, the WUI land surface imposes a heterogeneous forcing of heat and momentum on the Atmospheric Boundary Layer (ABL), making the understanding and prediction of WUI fire more difficult. Wildfire-atmosphere models have been used in the fire community to understand wildfires. Traditionally, wildfire models are constructed using either physical or empirical approaches (Bakhshaii & Johnson, 2019). The physical models focus on the fundamental physics of combustion and fire spread (A. L. Sullivan, 2009a). In contrast, the empirical models are based on analytical statistics of the rate of spread obtained from observations or experiments (A. L. Sullivan, 2009b). With technological advancements and model development, a new generation of wildfire models has been developed to include atmospheric conditions in the physical and empirical fire models. This is usually done by coupling a fire model to a numerical weather prediction (NWP) model or a computational fluid dynamics (CFD) model (Bakhshaii & Johnson, 2019). As summarized by Bakhshaii and Johnson (2019), these new generation wildfire-atmosphere models include FIRETEC (Linn et al., 2002), the Wildland-urban interface Fire Dynamics Simulator (WFDS) (Mell et al., 2007), Coupled Atmosphere-Wildland Fire-Environment (CAWFE) (Clark et al., 1996b, 1996a, 2004; J. Coen, 2013), the Weather Research and Forecasting (WRF) system combined with a wildfire module (WRF-FIRE) (J. L. Coen et al., 2013; Mandel et al., 2011; Patton & Coen, 2004), the Advanced Regional Prediction System (ARPS) coupled with DEVS-FIRE (Dahl et al., 2015), and ForeFire/Meso-NH (Filippi et al., 2011, 2013). In addition to these models, FireFOAM (fireFoam dev, 2023; Trouvé & Wang, 2010; Wang et al., 2011) has been developed as a fire modelling extension within the OpenFOAM toolbox (<https://www.openfoam.com/>; last access: 31 May 31, 2024). The Parallelized Large Eddy Simulation Model (PALM) has also been used for fire research (Dal-Ri dos Santos



Figure 1. Maps and images depicting the location and landscape of the Bottle Lake Forest (BLF) area in Christchurch, New Zealand. Bottom left: Maps of New Zealand and Christchurch (©MapTiler and ©OpenStreetMap). Top left: Satellite imagery of the BLF area (©Google Earth). The yellow pin indicates the location of a SoDAR (Sonic Detection And Ranging) operated between November 2022 and April 2023. The blue pin marks the location of the automatic weather station (AWS) operated by Fire Emergency New Zealand (FENZ). Top right: zoomed-in image of the WUI. For the scale reference, the approximate length of 100 m is shown between the edge of the forest and the residential area. Bottom right: a 3D map of the landscape in the BLF WUI rendered on top of the satellite imagery. High topography is colored in orange, the forests are colored in green, and the buildings are plotted as white 3D blocks. Map data contain Christchurch 1 m digital surface data (Environment Canterbury Regional Council, 2020).

& Yaghoobian, 2023; Zhang et al., 2023). These coupled models are useful for a better understanding of and to gain more insights into fire-atmospheric dynamics and interactions.

To capture the realistic weather conditions, the microscale ABL flows, and the high-resolution landscape of WUI, we have used PALM in this study to investigate the fire-atmosphere dynamics in the BLF WUI. PALM is an open-source Large Eddy Simulation (LES) model that enables very fine (grid spacing ≤ 1 m) simulations for atmospheric and ocean research (Maronga et al., 2015, 2020). With its offline-nesting module, PALM can include realistic weather conditions obtained from NWP models (Kadasch et al., 2021; Lin et al., 2021). Several features have been developed in PALM to resolve land surface physics covering the two key factors of WUI: the urban surface model (Resler et al., 2017) for the urban built-ups, and the plant canopy model (Maronga et al., 2020) for the wildland forest canopy. High-resolution geospatial information of WUI can be easily integrated into PALM using community-developed modeling tools (e.g. Heldens et al., 2020; Lin et al., 2024, and citations therein). Given PALM’s high adaptability, many studies have used it to better understand the ABL flows in urban (e.g. Belda et al., 2021; Kurppa et al., 2020; Salim et al., 2022; Vogel et al., 2022; Wolf et al., 2020) and forest environments (e.g. Kanani-Sühring & Raasch, 2017; Neves et al., 2018; Serra-Neto et al., 2021; Zhang et al., 2022). PALM has been used to investigate fire-atmosphere turbulent energy transport (Zhang et al., 2023) and the impact of an idealized urban boundary layer on firebrand transport (Dal-Ri dos Santos & Yaghoobian, 2023). However, no former studies have examined the impact of WUI on fire-atmosphere dynamics using a high-resolution turbulence-resolving model like PALM.

In this study, we investigate how the presence of the BLF WUI influences the atmospheric flows in the ABL and the fire-atmosphere dynamics. Section 2 describes the model and the design of the experimental case study. Section 3 examines the simulation results of fire heat transport, the flow characteristics, and the evolution of the ABL. The results of this study are further discussed in Section 4, along with future aspects. The conclusions of this paper are given in Section 5.

2 Model configuration and experiment design

PALM version 22.10 is used in this study. PALM solves the turbulent flow based on the non-hydrostatic incompressible Navier-Stokes equations under the Boussinesq approximation (Maronga et al., 2015). The assumption of incompressibility is appropriate for fire-atmosphere interaction simulations (Tang, 2017; Zhang et al., 2023). The turbulence closure is based on a modified three-dimensional Deardorff 1.5-order scheme, assuming a proportional relationship between the energy transport by sub-grid-scale eddies and the local gradient of the average quantities (Deardorff, 1980; Maronga et al., 2015).

The domain configuration of simulations conducted in this study is shown in Table 1 and Figure 2. The data sets and tools used to produce the PALM static geospatial information input are identical to those described in Lin et al. (2024). The first domain (D01) has flat terrain only with a homogeneous land use type of grassland. Christchurch is mainly surrounded by grassland. The flat terrain domain is designed to transfer synoptic forcing to the child domains while preventing numerical instability stemming from steep terrain near the lateral boundaries (Lin et al., 2023). Regarding the nested domains, the second domain (D02) only includes topography with land use information derived from the New Zealand Land Cover Database (LCDB) V5.0 (Landcare Research, 2020). In addition to topography and land use information, the third and fourth domains (D03 and D04) include information on pavements and streets, buildings, and plant canopy. All domains switched on the radiative transfer model (Krč et al., 2021) and the land surface model (Gehrke et al., 2021). Only D03 and D04 include the urban surface (Resler et al., 2017) and plant canopy models (Maronga et al., 2020). The landscape of D04 is shown in Figure 2b. The forest area in D04 can be identified by a high leaf area index ($LAI > 2.5 \text{ m}^2 \text{ m}^{-2}$). We focus on D04 for analysis and discussions.

Table 1. PALM domain configuration.

Domain	Number of grid points (x, y, z)	Domain size (x, y, z)	Horizontal grid spacing (dx, dy)	Vertical grid spacing (dz)
D01	324*324*192	11664 m *11664 m *6912 m	36 m	36 m
D02	216*216*144	7776 m*7776 m*5184 m	36 m	36 m
D03	360*360*360	4320 m*4320 m*4320 m	12 m	12 m
D04	468*612*648	1872 m*2448 m*2592 m	4 m	4 m

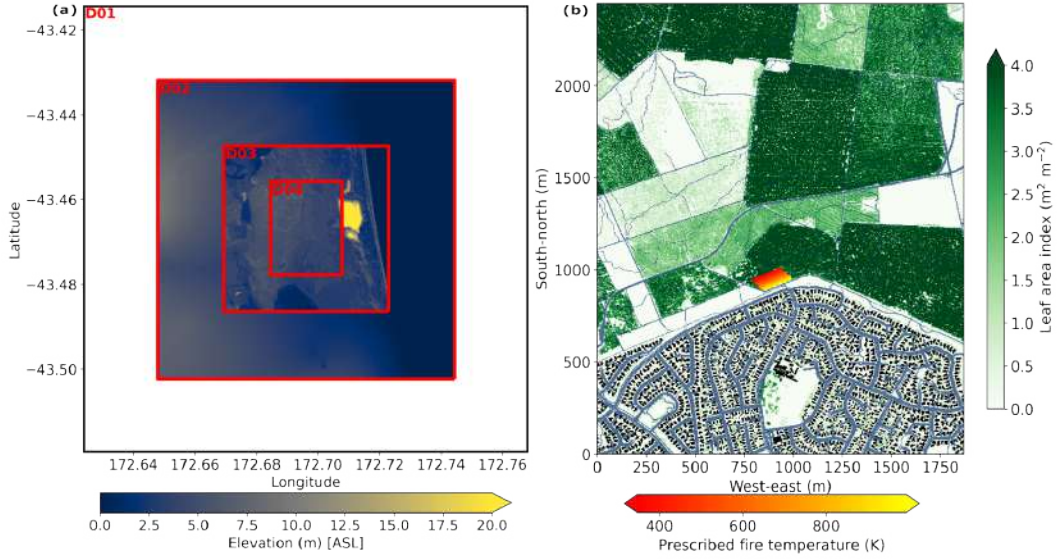


Figure 2. (a) A topographic map (elevation above sea level) showing the PALM simulation domain configuration. The simulation includes four nested domains (D01, D02, D03, and D04). D01 is a flat terrain domain. (b) Land use information of D04: the forest is marked by leaf area index (LAI) in green, buildings are shown in black, and pavements and streets are colored in light blue. The red patch marks the location of the prescribed temperature, representing fire.

To reproduce fire weather, we examined the fire weather index (FWI) during the 2022/2023 New Zealand fire season. The FWI was calculated based on data obtained from an automatic weather station (AWS) located in the BLF area operated by Fire Emergency New Zealand (FENZ) (location see blue pin in Figure 1). The data are freely accessible via the New Zealand Modeling Consortium Open Environmental Digital Library (envlib.org; last access 6 June 2024). The 5th of February, 2023, was identified as a high FWI day. The FWI was around 24.3, which is the second highest between December 2022 and May 2023. This number is above the median FWI for high-fire weather days in the BLF area (see long-term analysis in Brody-Heine et al., 2023). The high FWI on 5th February 2023 coincides with a foehn event picking up in the late afternoon, bringing strong and dry north-westerlies over Christchurch. A SoDAR (Sonic Detection And Ranging; location see yellow pin in Figure 1) was operating inside the BLF area between November 2022 and April 2023. It recorded wind speed of approximately 4.4 m s^{-1} near the canopy top (approximately 30 m above ground level) and 25 m s^{-1} at around 300 m above ground level. With such weather conditions, fire is likely to occur, spreading from the forest into the residential area in the south.

Figure 3 shows the vertical profiles used to initialize the simulations. These profiles were obtained from the SoDAR (up to 450 m) and WRF simulations (above 450 m). The WRF simulations were operated and are hosted by the New Zealand Modeling Consortium (envlib.org; last access 6 June 2024). The long-wave and short-wave radiation fields were obtained from the WRF simulations for a more realistic representation of radiative forcings. All simulations started at 0700 UTC on 5th February 2023 (equivalent to 1900 local standard time), and the simulation time is 2.5 hours. The fire was switched on for the last 30 minutes of the simulation. The first hour of the simulations is considered as model spin-up. To understand the role of the WUI in fire-atmosphere dynamics, we conducted two sets of simulations. One has the full WUI environment, and the other has flat terrain with land use configured as grassland only for all nested domains. For each set of the simulations, a baseline simulation with no fire throughout the entire simulation was conducted along with a simulation with fire switched on after 2 hours into the simulation. Hereafter, we denote these simulations as WUI_Fire (WUI environment with fire switched on), WUI_Base (WUI environment with no fire), Flat_Fire (flat terrain with fire switched on), and Flat_Base (flat terrain with no fire).

The fire fields prescribed in the simulations were derived from an infrared overhead video acquired during an instrumented prescribed burn experiment that took place in Rakaia Gorge, Canterbury, New Zealand. An unmanned Aerial Vehicle (UAV) was used to acquire the footage, and the resulting temperature profile was compared with 25 in-situ temperature probes evenly spaced inside the experimental plot. For more details, readers are referred to Katurji et al. (2022); Valencia, Melnik, Kelly, et al. (2023); Valencia, Melnik, Sanders, et al. (2023). To derive a normalized temperature curve (hereafter the fire curve), 20,000 data points of brightness temperatures were analyzed from the infrared footage. Only measurements exceeding fireline intensities of 1000 kW m^{-2} were included to minimize errors related to footage stabilization and flame visualization. All measurements of brightness temperatures were adjusted to 100°C for consistency. The fire curve describing the fire temperature T_{fire} varying over the distance (x) takes the form of

$$T_{fire}(x) = 1.035 \frac{b}{a} * \exp\left(-\frac{x-c}{b}\right) - \exp\left(-\frac{x-d}{e}\right) * T_{peak} \quad [K] \quad (1)$$

where a , b , c , d , and e are least-square fitting coefficients. Their values are -0.135, -0.632, 1.782, 0.925, -0.036, respectively. T_{peak} represents the highest temperature of fire. Since we do not have the exact temperature curve for the pine forest, we obtained the normalized fire curve and prescribed the highest temperature of 993 K. The temperature of 993 K was selected based on the oak wood and pine wood fire brand temperature described in Dal-Ri dos Santos and Yaghoobian (2023); Matvienko et al. (2022); Tse and Fernandez-Pello

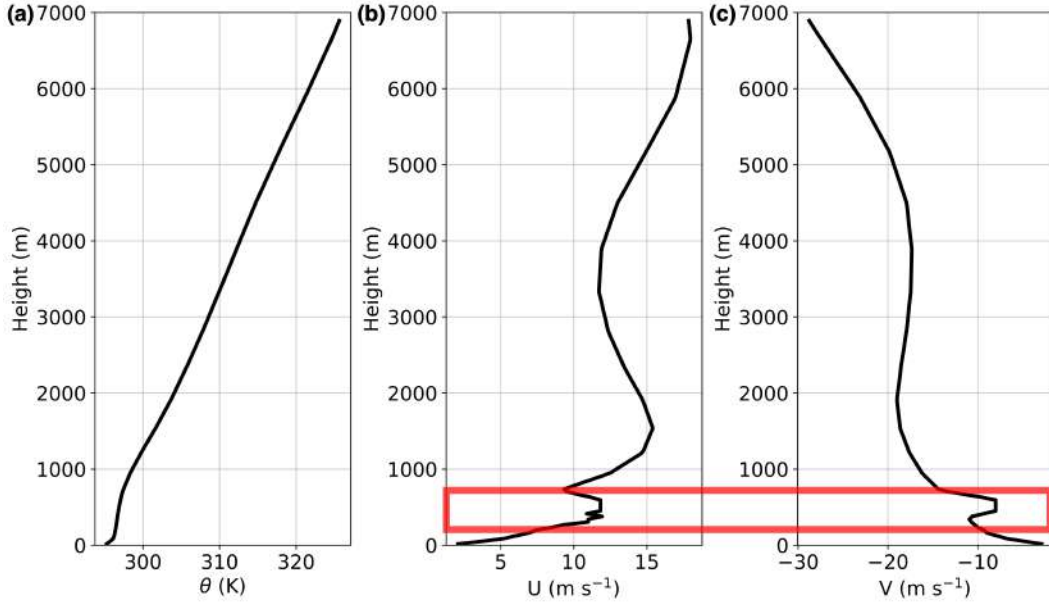


Figure 3. Vertical profiles of (a) potential temperature (θ), (b) u-component of wind, and (c) v-component of wind for simulation initialization. The red box marks the height of a strong wind shear observed by the SoDAR.

(1998). The temperature curve shown in Figure 4 represents the temperature characteristics of fire (preheating, combustion, and smoldering). However, it should be noted that in this study, we only prescribed part of the fire curve (gray box in Figure 4) as a representation of fire heat forcing only. This temperature field was prescribed from the surface to the height of the forest canopy. Similar to Zhang et al. (2023), the location of the prescribed heat forcing is static, and no initiation/combustion processes are discussed in this study. The implementation of the fire curve in the simulations is illustrated in Figure 2b.

3 Results

This section shows the simulation results. To investigate the flow characteristics in the BLF WUI, we compare the results between the WUI simulations and the flat terrain simulations. Analysis of the baseline simulations with the fire switched off is presented for the understanding of ABL evolution. The analysis presented in this section mainly focuses on the 30-minute period after the fire was switched on. Hereafter, the time within the simulations is reported in HH:MM:SS format relative to the start time, with “00:00:00” corresponding to the model initialization time (0700 UTC on 5th February 2023). Subsequent times are denoted in hours, minutes, and seconds from this start point, e.g., “01:40:50” for 1 hour 40 minutes and 50 seconds into the simulation (0840 UTC + 50 s) and “02:30:00” for 2.5 hours into the simulation (0930 UTC).

3.1 Fire in the WUI

Figures 5 and 6 show the horizontal cross-sections of potential temperature (θ), u , v , and w at 2 m above the surface for WUI_Fire and Flat_Fire, respectively. Here, instantaneous snapshots of three timestamps were chosen to demonstrate the dynamic and turbulent nature of the simulations. For readers interested in more details of the simulations, animations showing the entire fire simulation can be found in the supplements. One-minute averages

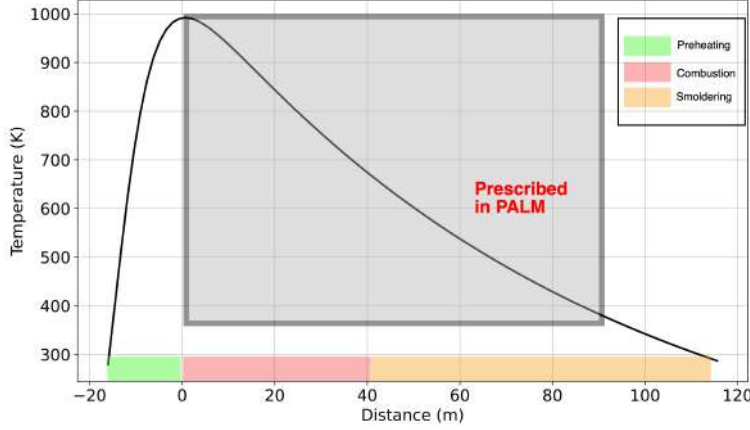


Figure 4. The fire temperature curve prescribed in the PALM simulations. The grey box indicates the temperature profile prescribed in the simulations to represent fire. The three characteristics of the fire temperature curve are marked in green (preheating), red (combustion), and yellow (smoldering).

for Figures 5, 6, and 7 are shown in Figures S1-3, respectively. Refer to Figures S4-7 for the horizontal cross sections of the simulations at mid-canopy (14 m above the surface) and the canopy top (22 m above the surface). Note that PALM uses the Arakawa Cartesian grid staggering (staggered Arakawa C-grid, Harlow & Welch, 1965; Arakawa & Lamb, 1977), where the first level for w is 4 m. Here, we use the notation of 2 m for the convenience of communication. The horizontal component of winds (u and v) show similar patterns in WUI_Fire and Flat_Fire. The heat forcing of fire induces strong buoyancy, causing the flow to converge near the fire front. The east side of the fire coincides with a strong positive u , while u is strongly negative on the west side of the fire (Figure 5d-f and Figure 6d-f). This is similar in v that strong southerly can be identified in the south of the fire front, associating with strong northerly behind the fire (Figure 5g-i and Figure 6g-i). In terms of w , strong updrafts (positive w) are present at the fire front with downdrafts (negative w) near the west and east side of the prescribed heat patch (Figure 5j-l and Figure 6j-l).

However, one can notice that the presence of WUI significantly modifies the near-surface flows. The impacts of buildings and forests are visible in Figure 5. The second hour of the simulation (02:00:00) corresponds to the local sunset time. After this, the surface cools down as the simulation continues. This cooling is present in both WUI_Fire and Flat_Fire (Figure 5a-c and Figure 6a-c). The cooling is more significant in the forest compared to the urban area in WUI_Fire and the entire area in Flat_Fire (Figure 5a-c and Figure 6a-c). The WUI coincides with greater surface roughness compared to the flat terrain. The reduction of winds is more significant where the forest is dense ($\text{LAI} > 3.5 \text{ m}^2 \text{ m}^{-2}$ in Figure 2b). The flat terrain presents a more organized pattern in the downwind transport of heat and the downwind flows (u , v , and w). While the dominant ambient winds are north-westerlies, Figures 5 and 6 show a divergence of inflow ahead of the fire (south side). The fire introduces a strong easterly flow to its east (negative u in Figures 5d-f and Figures 6d-f), and a strong southerly flow to its south (positive v in Figures 5j-l and Figures 6j-l). The easterly and southerly components of winds in Flat_Fire are present over a smaller area than their counterparts (westerly and northerly components of winds, respectively). The patterns of w at the downwind side of the fire are almost symmetrical along the fire center line (dashed red line in Figure 6a) in Flat_Fire (Figure 6j-l). In contrast, in WUI_Fire, the areas associated with the easterly and southerly wind components are much larger, changing the wind patterns downwind of the fire with a scale of a few hundred meters.

The symmetrical patterns of w at the downwind side of the fire are broken into cells of up- and downdrafts due to the obstructions of the WUI landscape. In Flat_Fire, the downwind transport of heat near the surface is similar across the three timestamps (Figure 6a-c), while WUI_Fire coincides with nearly no downwind transport of heat (Figure 5a), strong downwind transport of heat of approximately 200 m from the fire front (Figure 5b), and a downwind transport of heat of around 100 m from the fire front (Figure 5c). Hereafter, we refer to this turbulent and dynamic behavior in WUI_Fire as heat pulsing.

The vertical cross-sections of θ and w along the fire are shown in Figure 7. The heat pulsing near the surface is visible in the vertical cross-sections of WUI_Fire (Figure 7a-b), but is absent in Flat_Fire (Figure 7e-f). In Flat_Fire, most of the heat goes upwards due to buoyancy, transporting little heat toward the surface and downwind. In contrast, WUI_Fire shows a strong downdraft at the fire front with downwind transport of heat towards the buildings (circled area in Figure 7b). In the snapshots shown in Figure 7, one can notice that the heat plume in WUI_Fire tilts more towards the surface with a more scattered structure, while the heat plume in Flat_Fire is more contained. The structures of w differ between the two simulations, too. Strongly positive w is presented in Flat_Fire (Figure 7g-h), whereas WUI_Fire coincides with negative w around the heat plume. The locations of negative w in Figure 7c-d resemble the locations where the heat plume ($\theta \geq 300$ K) is absent in Figure 7a-b. Near the surface, WUI_Fire shows cells of weakly negative w from the fire front to 600 m in front of the fire. This weakly negative w is only present after 400 m in front of the fire in Flat_Fire. It should be noted that the south side of the BLF canopy height is approximately 22 m above the ground. These snapshots shown in Figures 5, 6, and 7 illustrate that the WUI changes the way fire and atmosphere interact and, subsequently, the downwind transport of heat from the fire.

Due to the turbulent nature of LES, different results could be produced at every single time step. Instantaneous snapshots do not conclude the general feature of the simulations. Therefore, we present Figure 8 to summarise the downwind impact of fire. Figure 8 shows the percentage of time that a grid point sees an increase in θ of more than 1 K after the fire is switched on. The temperature difference was calculated by subtracting a fire simulation from its baseline counterpart. The total time of the fire is 1800 seconds, and one-second output is used in this analysis, allowing sufficient data points for this kind of analysis. This analysis gives us an overview of the heat footprints, showing the potential downwind impact of fire heat. The footprints were calculated for both 2 m above the surface and near the canopy top (22 m above the surface). Refer to Figure S8 for footprints at mid-canopy. We picked the two streets in front of the fire to reference the distance and the impact of the downwind heat. Willoughby Lane (WLN) is approximately 45 m in front of the prescribed fire, and down to the south-east of WLN is Anglesea Avenue (AAV). The locations of WLN and AAV are marked by dashed and solid red lines in Figures 8a-d, respectively. AAV is around 95 m away from WLN.

In general, the heat footprints are more spatially confined near the location of the prescribed fire in Flat_Fire, occupying a smaller, more defined area in both the horizontal and vertical directions (Figure 8a,c, and e). Figures 8a and 8c show that almost no heat is transported to AAV near the surface, and little heat reached over AAV at the canopy top. The shape of Flat_Fire footprints shows a dual-peak structure at both 2 m and 22 m above the surface, with a longer distance of downwind heat transport near the west and east sides of the fire and a shorter distance near the center line. The footprints at 22 m (Figure 8c) have a more symmetrical structure, which resembles the symmetrical patterns in w as shown in Figure 6. In WUI_Fire, the downwind heat reaches AAV from the surface to the canopy top (Figures 8a and 8d). The near-surface footprints in WUI_Fire (Figure 8b) do not show a dual-peak pattern as in Flat_Fire (Figure 8a). The density of the footprints decreases with distance ahead of the fire, encompassing high values of 75% close to the center line of the fire patch near WLN. The dual-peak pattern, however, is noticeable at the canopy height in WUI_Fire for values greater than 87% (Figure 8d). We consider this as an indication that

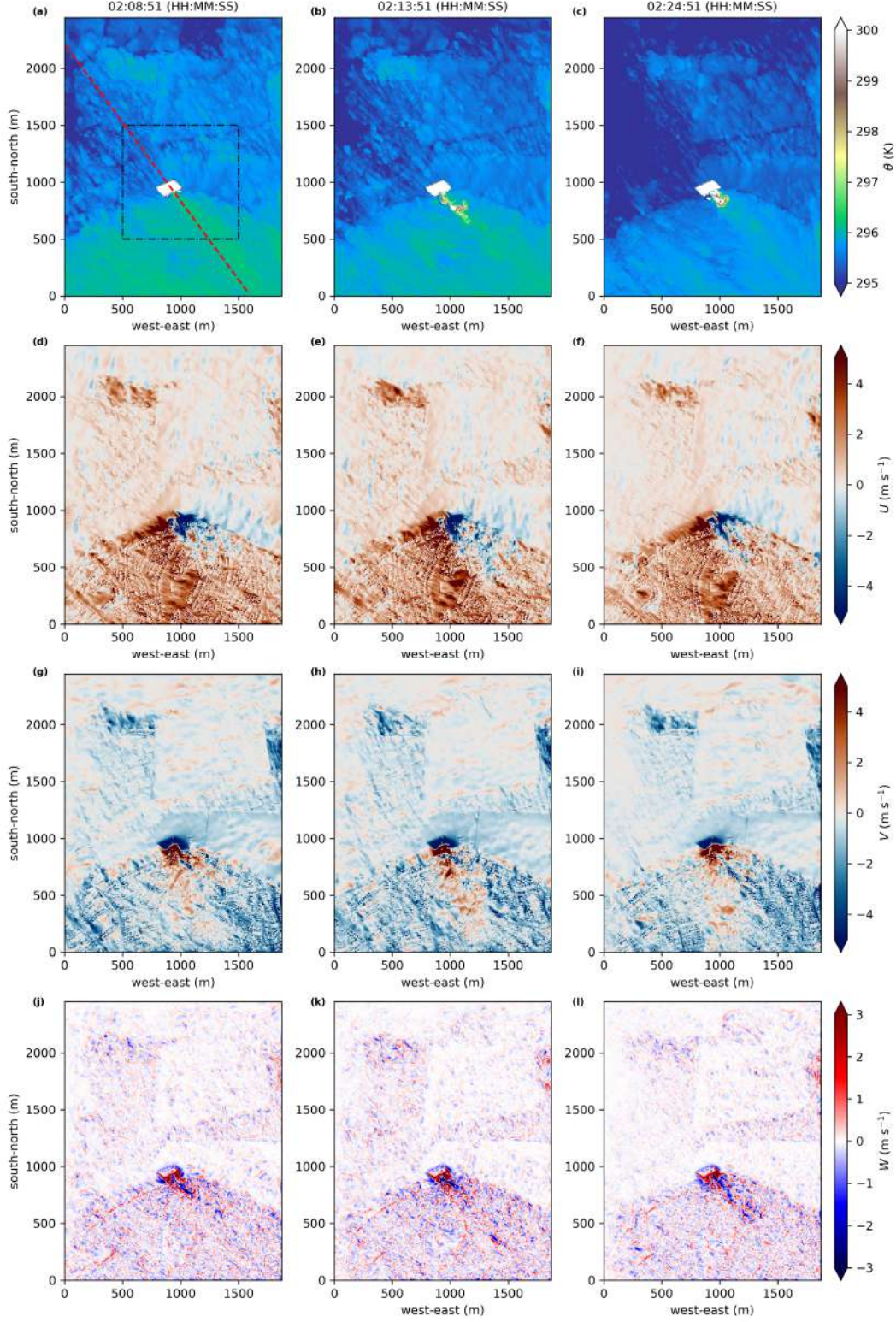


Figure 5. Instantaneous snapshots showing horizontal cross sections of θ (a-c), u (d-f), v (g-i), and w (j-l) at 2 m above the surface obtained from WUIFire. From left to right, the first column is for 02:08:51, the second column for 02:13:51, and the third column for 02:24:51. Here, timestamps represent the hours, minutes, and seconds relative to the start time of the simulation. In panel (a), the dashed red line indicates the location of vertical cross sections shown in Figure 7. The dashed black box marks the area shown in Figure 8.

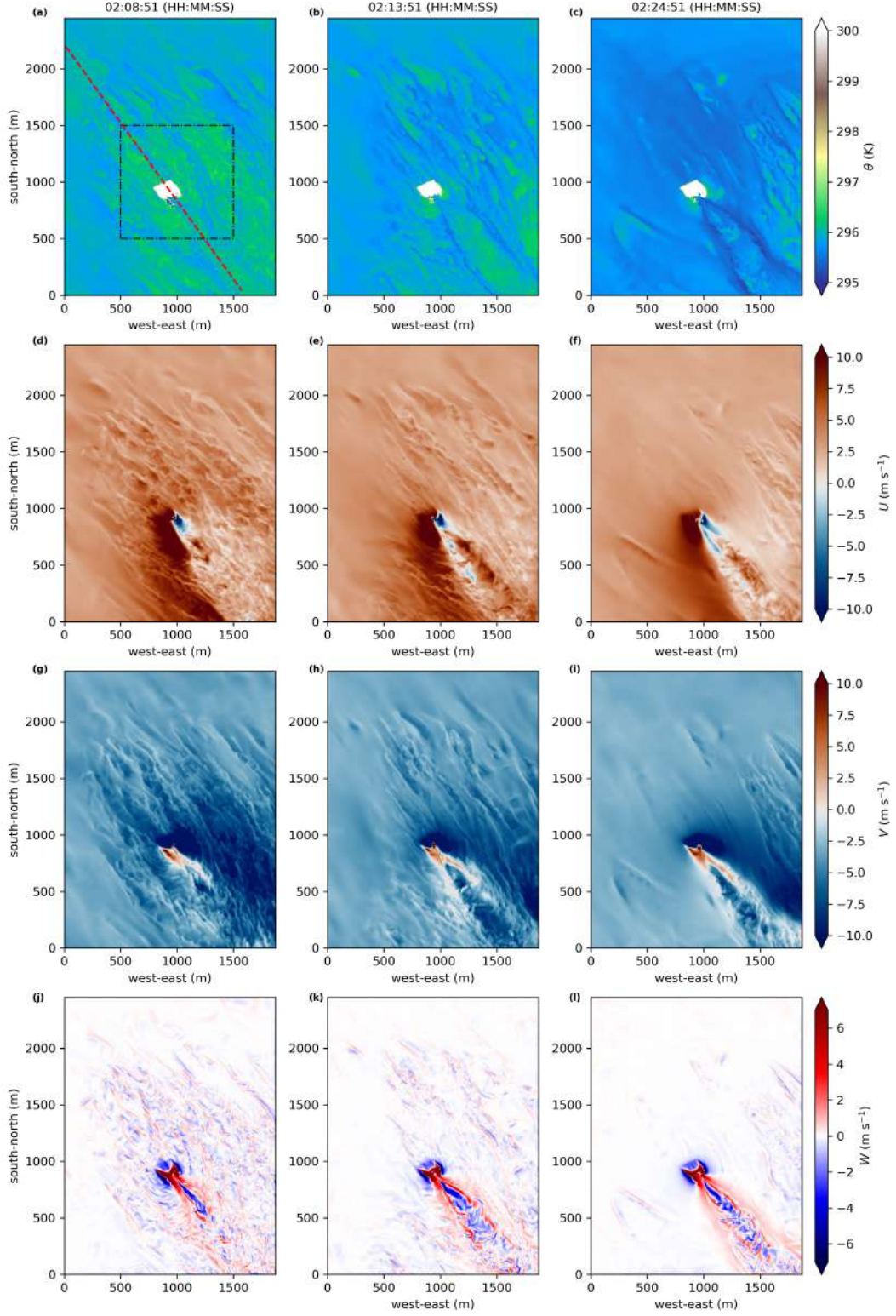


Figure 6. Similar to Figure 5, but for the Flat.Fire simulation. Note the differences in the colormap scales compared to Figure 5.

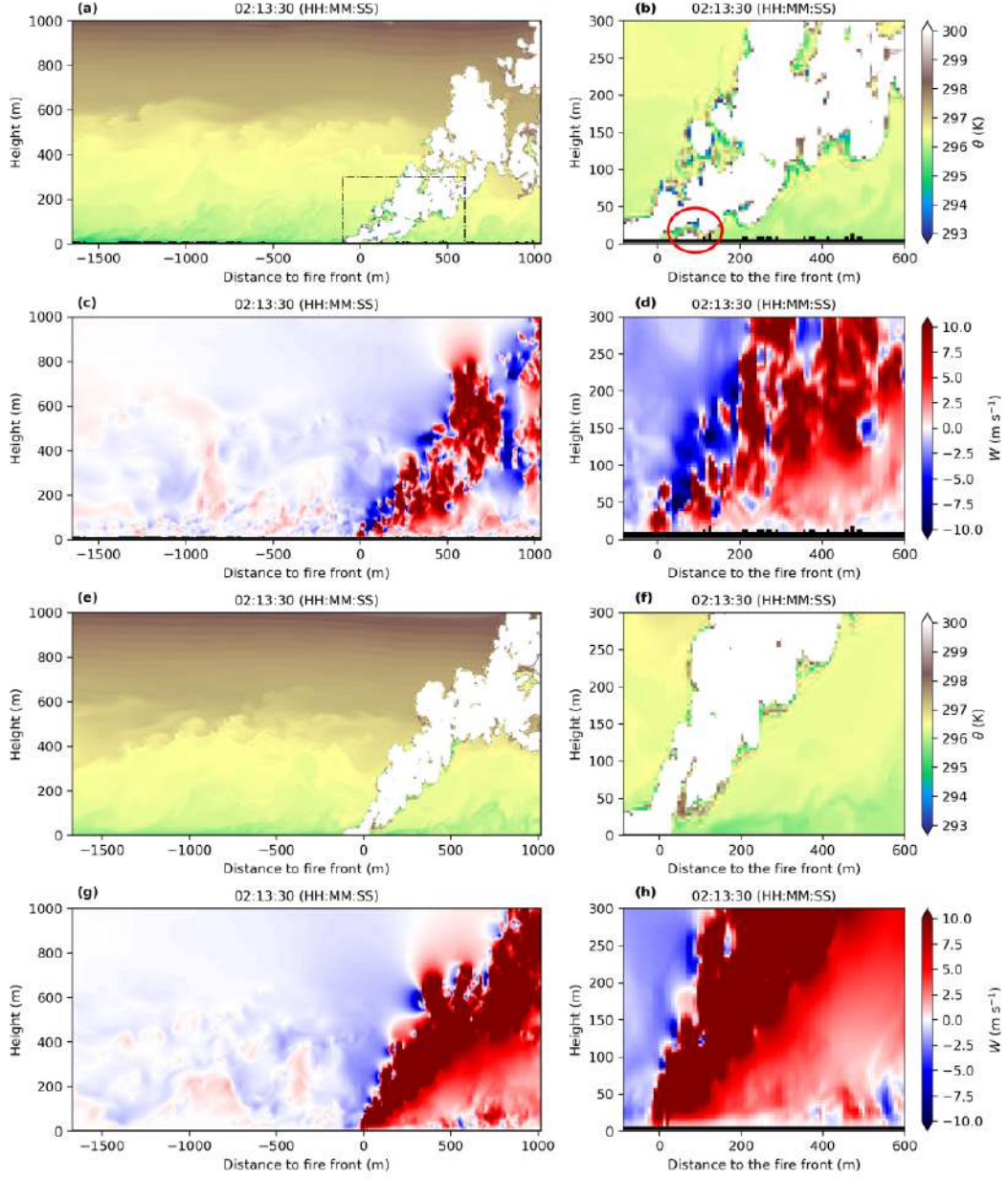


Figure 7. Instantaneous snapshots at 02:13:30 showing vertical cross sections obtained from WUI_Fire (a-d) and Flat_Fire (e-h). Panels (a-b) and (e-f) are for θ . Panels (c-d) and (g-h) are for w . The first column shows the entire vertical cross-section up to 1000 m high, and the second column is a zoomed-in of the first column. The zoomed-in area is marked by the dashed black box in (a). The red circle in (b) highlights the downwind heat transport near the surface in WUI_Fire. The black rectangles near the surface in (a-d) are buildings. The location of the vertical cross-sections is shown in Figures 5a and 6a.

the impact of the WUI surface decreases with height. Despite such a decrease, the impact of the WUI on the fire-atmosphere interactions does not simply diminish above the canopy height. As shown in Figure 8e and 8f, the heat plumes travel much further downwind at all heights in WUI_Fire than those in Flat_Fire. Some of the plume-affected areas have an occurrence rate of more than 63%, equivalent to 19 minutes. The results shown here are in agreement with Figure 7. The vertical footprints of the heat plume bend more towards the surface in WUI_Fire than those in Flat_Fire.

3.2 WUI flow characteristics

To further explore the impact of WUI and the dynamics at the downwind side of the fire, time series of θ and winds at WLN and AAV are presented in Figure 9. The time series were obtained at two heights: 2 m and 22 m above the surface. The time series for mid-canopy is presented in Figure S9. Mean values were derived for WLN and AAV at the locations marked in Figure 8. Note that in Figure 9e and 9m, the time series of θ for AAV appear to be straight lines due to the difference in the scale of fire-impacted temperature and the ambient atmosphere temperature. The downwind heat barely reaches AAV (as shown in Figure 8a and 8c). In Flat_Fire, with a high concentration of heat transported to WLN, θ is well above 400 K most of the time at 2 m and 22 m (Figure 9e and 9m). In WUI_Fire, however, the heat is more sparsely distributed downwind, leading to a less intense increase in temperature (below 400 K at 2 m). The heat pulsing can be identified in Figure 9 that the temperature increase in WUI_Fire coincides with short-lived spikes while the increase in Flat_Fire is long-lasting and more steady. As WLN is closer to the fire than AAV, it shows a stronger impact from the fire.

Before the fire is switched on, the magnitude of winds in WUI_Fire is smaller than that in Flat_Fire due to a higher surface roughness associated with the WUI. After the fire is switched on, the changes in the winds in WUI_Fire differ significantly from those in Flat_Fire at both the surface and the canopy height. Near the surface, both WLN and AAV in WUI_Fire have a strong shift to negative in u (easterly; Figure 9b), whereas this negative shift in u is weaker in Flat_Fire (Figure 9f). Regarding v , in WUI_Fire, both WLN and AAV show a strong shift to southerlies (positive v ; Figure 9c), with a greater magnitude at WLN. On the contrary, Flat_Fire shows a strong northerly shift of v at WLN (Figure 9g), with v fluctuating around 0 m s⁻¹ approximately 2 minutes after the fire was switched on. w in Flat_Fire rises markedly to over 5 m s⁻¹ at WLN after the fire was switched on (Figure 9h). The magnitude of such a rise is weaker at AAV with a magnitude of about 2 m s⁻¹ at maximum. The increase in w in WUI_Fire is less steep (Figure 9d), while the time series show noticeable periods of negative w at WLN and AAV. The time series near the canopy height (Figure 9i-p) generally show a similar pattern compared to their 2 m counterparts. However, the intensity of the changes in the winds varies. In WUI_Fire, u exhibits a more pronounced easterly shift at WLN, with westerlies being recorded occasionally. At AAV, the magnitudes of u are greater than those at 2 m, while the mean flow centers around 0 m s⁻¹ (Figure 9j), indicating a weaker easterly transition compared to u at 2 m (Figure 9b). For WUI_Fire, the time series of u at AAV also centers around 0 m s⁻¹, whereas u turns to strong westerly at WLN (Figure 9n), which is opposite to the same u at 2 m (Figure 9f). In terms of v , WUI_Fire shows that the positive maxima are comparable near the surface and near the canopy top, while v ramps down from positive (southerly) to negative (northerly) more markedly at the canopy top (Figure 9k). However, the time series of v in Flat_Fire only show a slight northerly displacement at the canopy top (Figure 9o) compared to those near the surface (Figure 9f). Moving further from the surface, the vertical motion gets stronger. At the canopy height, the upward motion intensifies at WLN in both WUI_Fire and Flat_Fire (Figure 9l, p). The amplification of the vertical motion with height is less notable for AAV in Flat_Fire, suggesting a weaker downwind fire impact. In contrast, AAV in WUI_Fire is associated with higher values of w (both positive and negative; Figure 9l). In general, the fire-impacted flows in WUI_Fire present a more significant transition against

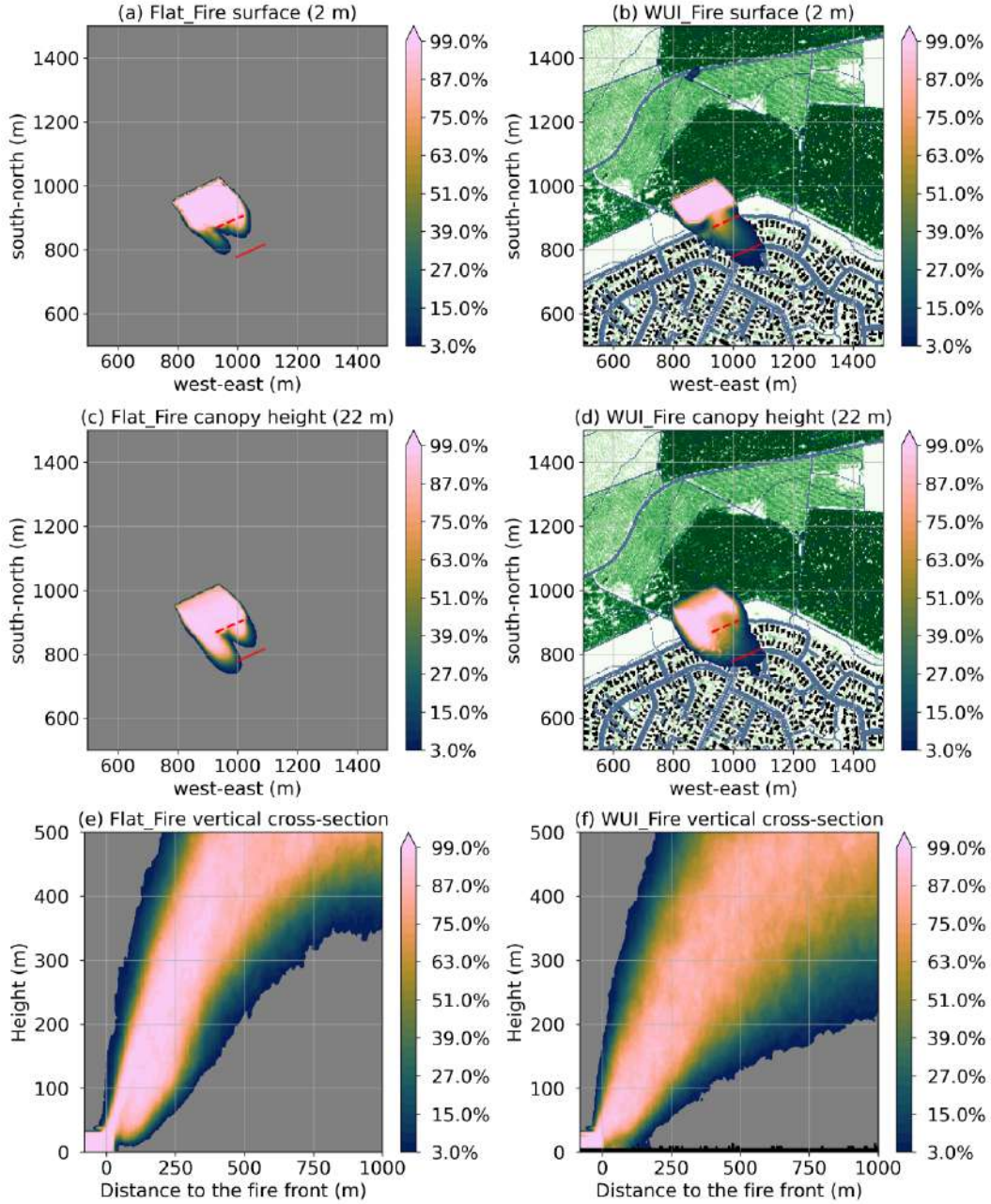


Figure 8. Percentage of occurrence when temperature increase of 1 K is captured at each grid point, comparing fire simulations to their baseline counterparts. Panels (a-b) are for 2 m above the surface, panels (c-d) are for the canopy height (22 m), and panels (e-f) are for the vertical cross-sections shown in Figure 7. The first column is for the flat terrain simulations, and the second column is for the WUI simulations. The WUI landscape of Figure 2b is shown in (b) and (d). Refer to Figures 5a and 6a for locations of (a-d). The dashed and solid red lines in (a-d) indicate the location of Willoughby Lane (WLN) and Anglesea Avenue (AAV), respectively. The distance between the two streets is approximately 95 m.

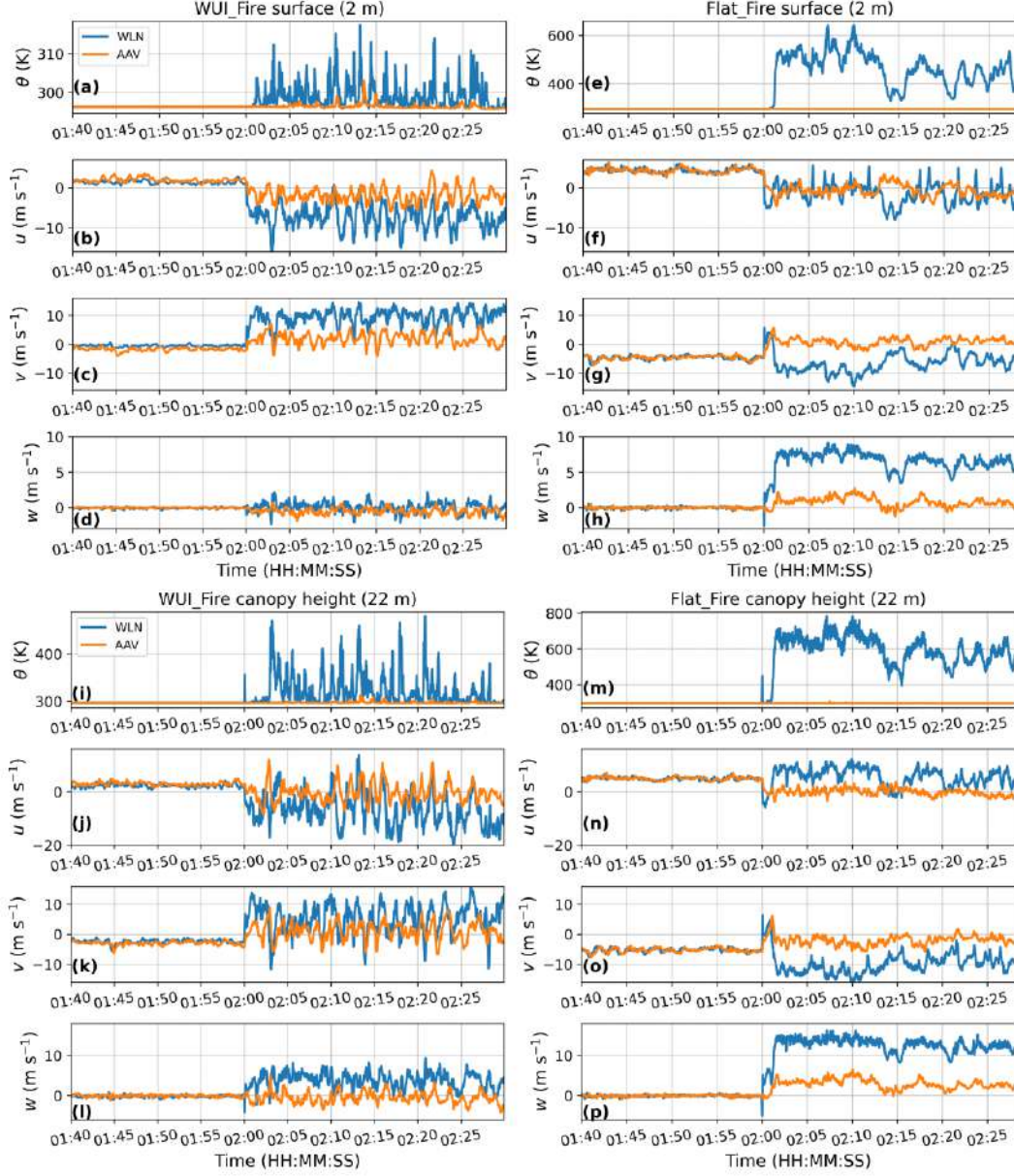


Figure 9. Time series of θ , u , v , and w for WLN and AAV at 2 m (a-h) and 22 m (i-p) above the surface. The first column is for WUI_Fire, and the second column is for Flat_Fire. Refer to panels (a) and (i) for color legends. The time series are areal means obtained from grid points marked by the dashed (WLN) and solid (AAV) red lines shown in Figure 8.

the ambient atmospheric flow (northwesterly) than their Flat_Fire counterparts. This agrees with the fact that the WUI modifies fire-atmosphere interactions substantially.

To examine the WUI flow characteristics more extensively, violin plots of u , v , w , and turbulence kinetic energy (TKE) at 2 m and 22 m above the surface are shown in Figures 10 and 11. The violin plots for mid-canopy are illustrated in Figure S10. These violin plots compare the last 30 minutes of baseline simulations and fire simulations to investigate the impact of the fire. Based on the dominant land use, D04 was classified into three parts: forest, interface, and urban. The details of the land use classification are shown in Figure A1. This classification is done based on the satellite imagery shown in Figure 1 and the New Zealand Land Cover Database (Landcare Research, 2020). The north of D04 is covered by the wildland forest, the south of D04 is the residential area with urban built-ups, and the grassland between the forest and the urban areas is considered the interface. Data for the entire simulation domain (denoted as All) are also presented in Figures 10 and 11 as a reference of the overall feature of the simulation. Note that the forest area has more data points than the interface and urban area. The violin plots are scaled such that the widest part is the maximum density.

All subplots in Figures 10 and 11 show an increase in the variable magnitudes when the fire is switched on. The impact of the fire is the least significant over the forest area in all simulations at both heights. The forest area is located upwind behind the prescribed heat source and hence experiences the least disturbances. Looking at 2 m above the surface, the amplification in u is the strongest in the interface, followed by the urban area in both WUI and flat terrain simulations (Figure 10a-b). In WUI_Base, u in the interface presents a higher median value, indicating an acceleration of the flow entering this area where the friction is lower (Figure 10a). In Flat_Base, the difference in u is subtle across the areas, since the surface roughness is homogeneous across the entire domain, and the only difference is the data extraction locations (Figure 10b). In Flat_Fire, u has a high distribution where $u > 8 \text{ m s}^{-1}$. This is absent in WUI_Fire. The figures of v show analogous patterns to u . The interface in the WUI simulations coincides with the most significant intensification of v wind velocity in both WUI_Base and WUI_Fire (Figure 10c). In Flat_Fire, one can notice a secondary peak in v distribution where $v < 6 \text{ m s}^{-1}$. This secondary peak appears in the location of the urban area in Flat_Fire, further downwind than the location of the interface (Figure 10d), but it is absent in WUI_Fire, where an urban surface is present. This suggests that the WUI interface prevents the development of a certain structure of the flow such that it aids a further downwind transport of heat, as shown in Figure 8. The violin plots of w show that the interface and the urban areas amplify the vertical motions of the flow (Figure 10e), which is absent in Flat_Base (Figure 10f). Nevertheless, in the fire simulations, the impact of WUI is less pronounced in w , while the intensification of w grows from the interface to the urban areas (along the downwind direction). This may be because of the fact that violin plots only capture the bulk characteristics of the flow. The characteristics of w may require a more detailed analysis of its turbulent features, where instantaneous snapshots, like Figures 5 and 6, should be considered. This is out of the scope of this paper. In Figures 10g-h, the fire simulations present a notable intensification of TKE compared to their baseline counterparts. This is expected due to the extra heat forcing introduced into the fire simulations. In WUI_Base, high TKE is exhibited in the interface compared to the forest and the urban areas (Figures 10g). Moreover, in WUI_Fire, the increase in TKE is strongest in the interface, followed by that in the urban. This is similar in the flat terrain simulations, while the amplification of TKE in the location of the interface is comparable to that in the location of the urban (Figures 10h). The magnitude of TKE is higher in the WUI simulations compared to their flat terrain counterparts. This supports our assumption that the WUI modifies the downwind flow, and hence, the downwind heat transfer is able to reach further away from the fire.

At the canopy height (22 m; Figure 11), the violin plots for u and v (Figure 11a-d) resemble those near the surface (2 m; Figure 10a-d), except that the magnitudes are greater.

It is noticeable that the forest area sees more changes when the fire is on, especially in v . This indicates that fire could interact with the ambient atmosphere upwind. This interaction may grow with height but is relatively weak. Regarding w , in the WUI simulations, WUI_Fire shows a slightly negative shift in urban compared to WUI_Base (Figure 11e). Such shift towards negative w is barely noticeable in Flat_Fire (Figure 11f). Moving from the surface to the canopy top, TKE rises in the WUI simulations (Figure 11g). In contrast to TKE at 2 m, TKE at 22 m in WUI_Fire is the highest in urban, followed by the interface. In the flat terrain simulations, the change in height does not show considerable changes in TKE (Figure 11h). This again suggests that the presence of WUI may aid the heat and energy transport away from the fire.

3.3 Evolution of the boundary layer

The ambient atmosphere has been identified to have an impact on the fire-induced flows (e.g. Sun et al., 2009; Kiefer et al., 2015; Zhang et al., 2023). In the instantaneous snapshots of vertical cross-sections shown in Figure 7, one can notice a wave-like structure between 400 m and 600 m in height. This location mirrors the wind shear location shown in Figure 3. These waves are recognised as Kelvin-Helmholtz waves (hereafter KH waves) induced by the strong wind shear. As shown in Figure 3a, the simulations were initialised with a stable surface layer, a near-neutral layer below 600 m, and a stable layer above 1000 m. These conditions are favourable for the formation of KH waves (e.g. Jiang et al., 2017; Dong et al., 2023). For readers' interest, an animation showing vertical cross-sections (as in Figure 7) of the entire fire simulation is provided in the supplements. Here, we only analyse the mean vertical structure of the boundary layer between the front of the fire and AAV for simplicity. The time series of vertical profiles of θ and anomalies of θ ($\theta'/\bar{\theta}$) are shown in Figure 12. The anomalies were calculated using a 5-minute rolling mean with a data frequency of 10 seconds.

As 02:00:00 is equivalent to the local sunset time (0900 UTC), WUI_Base and Flat_Base show cooling near the surface after sunset (Figure 12a-b). This cooling is less pronounced in Flat_Base due to its surface being configured as grassland only. The WUI surface enhances the stratification of air near the surface. The growth of the surface layer is more prominent in $\theta'/\bar{\theta}$. Before 02:00:00, $\theta'/\bar{\theta}$ is weak near the surface in WUI_Base and Flat_Base, mostly near zero and slightly positive (Figure 12c-d). The anomalies were strengthened after sunset. Negative phases of $\theta'/\bar{\theta}$ start to appear and the magnitude of $\theta'/\bar{\theta}$ increases to more than $\pm 1.3 \times 10^{-4}$. This growth of $\theta'/\bar{\theta}$ is stronger in WUI_Base than that in Flat_Base, meaning the WUI surface possesses stronger modification of the surface layer flows.

At higher levels, the 296.5 K lines shown in Figure 12a-b fluctuate around 400 m over time. This fluctuation is considered to be caused by disturbances from the KH waves shown in Figure 7. Although all simulations were initialised with the same meteorological profiles and radiative forcing, the profiles of the ambient atmosphere shown in Figure 12a (WUI_Base) and Figure 12b (Flat_Base) are not identical. However, the differences between WUI_Base and Flat_Base are difficult to identify from Figure 12a-b above 200 m. This is the same in $\theta'/\bar{\theta}$ (Figure 12c-d). The locations of warm and cold anomalies vary over time. For example, at 01:40:00, WUI_Base coincides with a cold anomaly at 400 m and a warm anomaly around 250 m (Figure 12c), while Flat_Base shows the opposite (Figure 12d). These differences suggest that the WUI surface could have an impact on the ambient atmosphere, but this impact is relatively small and subtle. Despite such differences, both simulations show a wave-like structure of $\theta'/\bar{\theta}$. One can notice streaks of downdraft from 500 m towards the surface, fading around 200 m. Disregarding the size and intensity of the anomaly streaks, a warm anomaly streak is always followed by a cold anomaly streak, and vice versa. These wave-like downdrafts could potentially be a driver of the heat pulsing presented in Section 3.1, but they are not the main driver. First of all, this wave-like downdraft feature is exhibited in both WUI_Base and Flat_Base, but no fire pulsing is

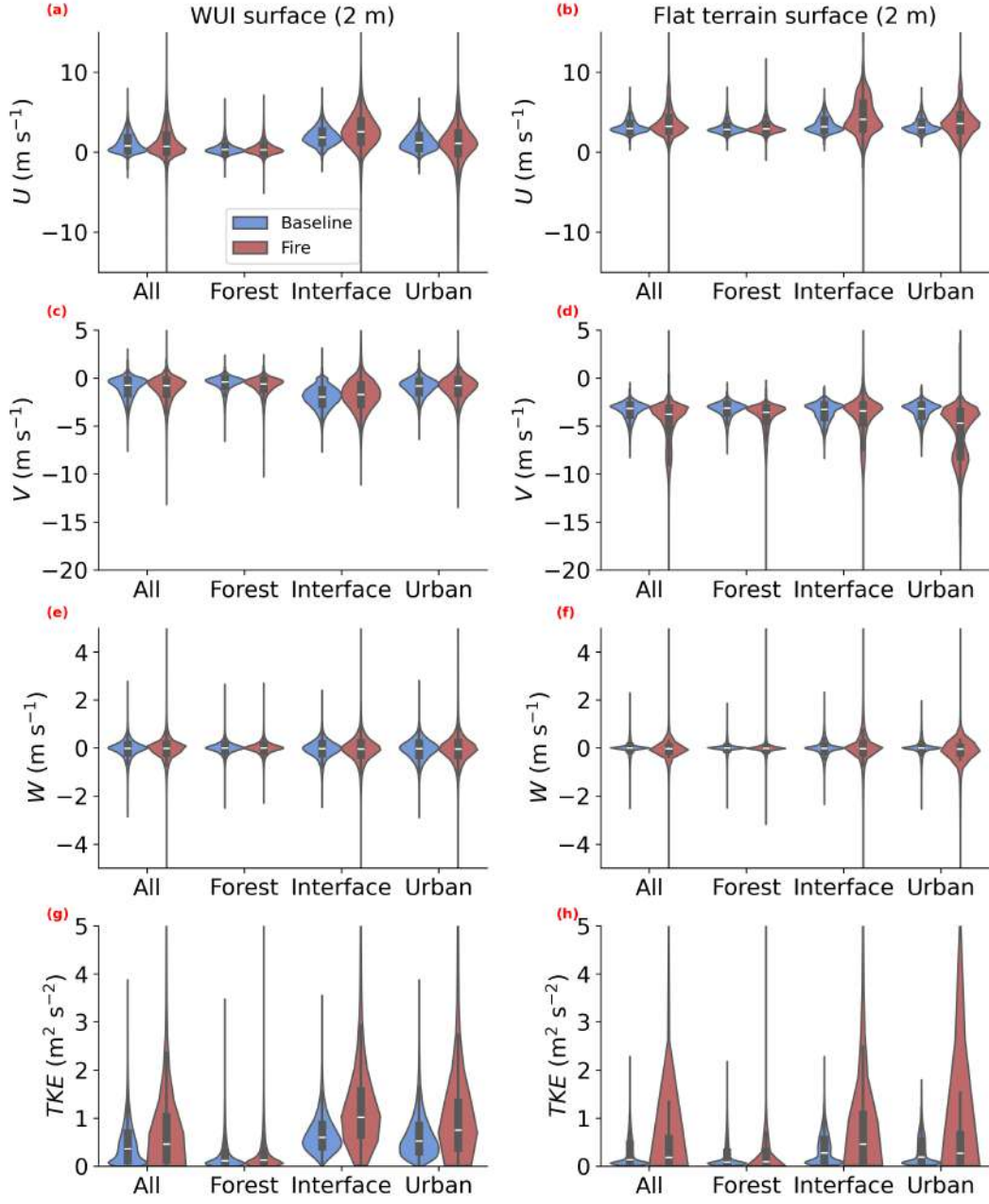


Figure 10. Violin plots comparing u (a-b), v (c-d), w (e-f), and TKE (g-h) at 2 m above the surface for the forest, interface, and urban areas between baseline simulations (blue) and their fire counterparts (red). The first column is for WUI simulations, and the second column is for flat terrain simulations.

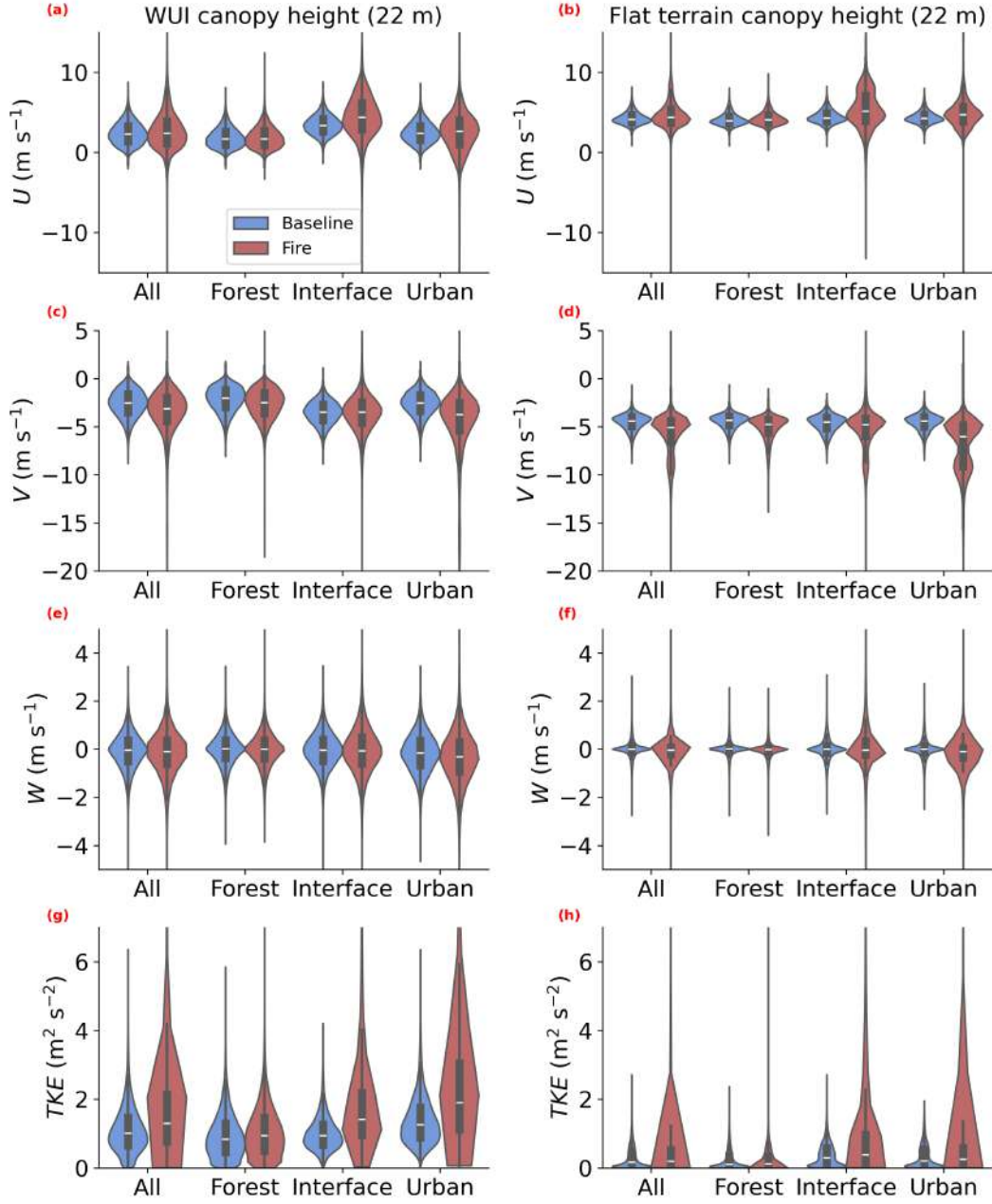


Figure 11. Similar to Figure 10, but for data obtained at 22 m above the surface.

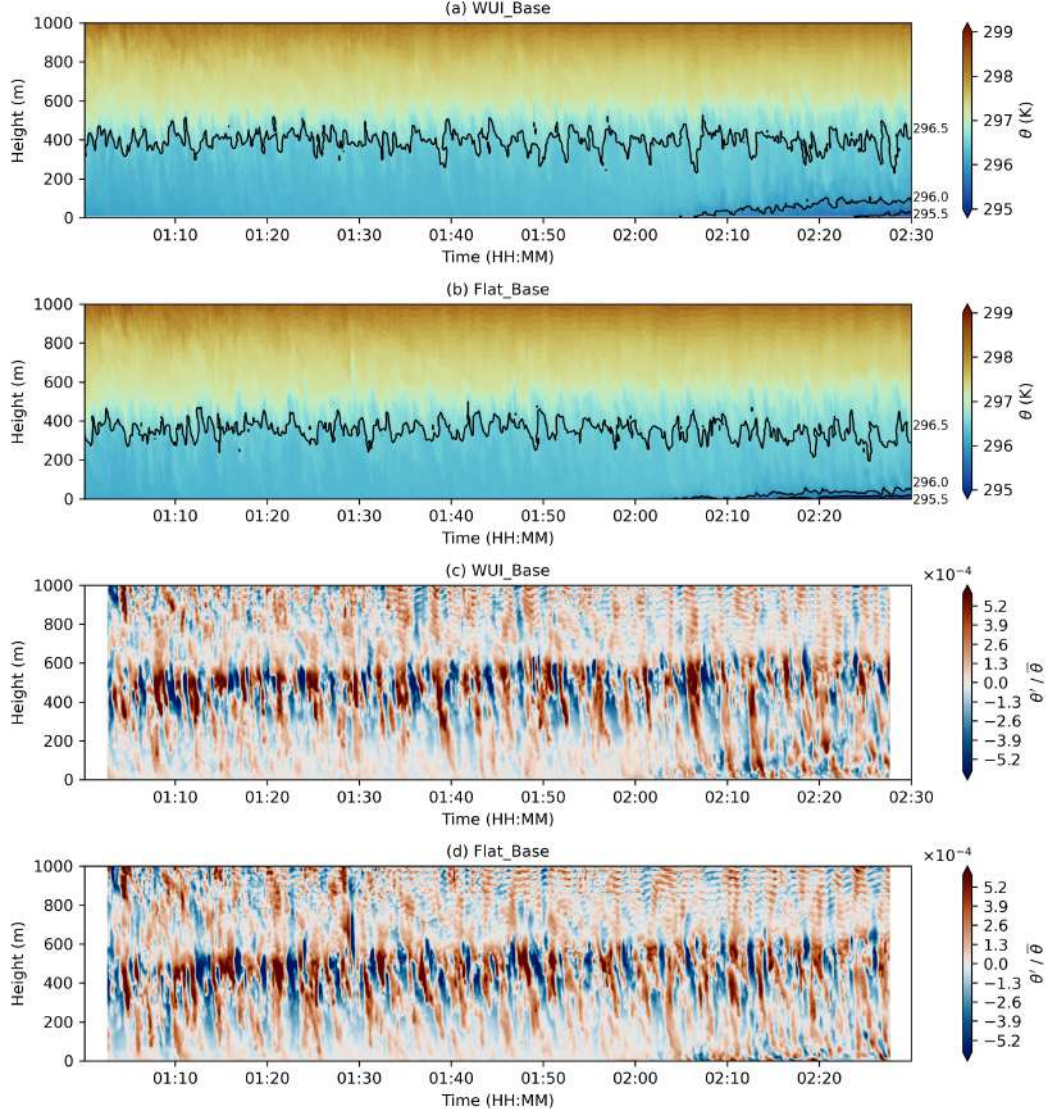


Figure 12. Time-height displays of θ (a-b) and $\theta' / \bar{\theta}$ (c-d). Panels (a) and (c) are for WUI_Base, and panels (b) and (d) are for Flat_Base. In (a-b), the black contour lines highlight θ of 295.5 K, 296.0 K, and 296.5 K (from bottom to top). These vertical profiles were taken from the vertical cross-sections along the fire center (Figure 7) between the front of the fire and AAV. A 5-minute rolling mean was applied to calculate the anomalies. Hence, no data were displayed for $\theta' / \bar{\theta}$ at the first and the last 5 minutes of the simulations.

observed in Flat_Base. Secondly, the cycles of these downdrafts (every 2-3 minutes) do not exhibit a clear correlation with the heat pulsing shown in Figures 9a and 9i.

However, we believe that the wave-like downdrafts induced by the KH waves are not insignificant for fire-atmosphere interactions. Given that the land use configuration is the only difference between the simulations, we believe that the WUI is the main factor that modifies the fire-atmosphere interactions. The presence of WUI induces heat pulsing and a further downwind transport of heat. The forcing from the WUI may intensify the interactions between the KH waves and heat plumes. More analysis is required to understand whether and how these wave-like features impact fire-atmosphere interactions. As this is out of the scope of this paper, we will discuss it as part of future work presented below.

4 Discussions and future aspects

Although we presented several aspects of the fire-atmosphere dynamics in the BLF WUI, many components have yet to be explored. One of the most intriguing questions surrounds the detailed dynamics causing the heat pulsing. In flat terrain, the upward motion and convergence of flow are strong around the fire, and most of the heat ascends with buoyancy. The horizontal cross-sections in Figure 6 show a relatively symmetric structure of the flow downwind. The violin plots (Figures 10 and 11) also present a secondary peak in u and v near the surface and at the canopy height downwind of the fire. Based on this evidence, we assume that there could be symmetric circulation diverging ahead of the fire that supports the upward motion of heat. The presence of WUI deconstructs the symmetric circulations and suppresses the upward motion.

It is, however, difficult to isolate each component of the BLF WUI due to its significant heterogeneity. The downdrafts caused by flows exiting the forest canopy could be considered as one of the factors. For example, Kiefer et al. (2016) found that forest gaps potentially impact the vertical and horizontal transport of heat away from the fire. Desai et al. (2024) investigated ramp-cliff structures in the temperature signal of forest canopy fires. In Figure 13 of Desai et al. (2024), they discussed that in a fire condition, the downdrafts at the forest edge could be stronger than those in no-fire conditions, leading to steeper drops in the temperature ramp-cliff structures. Different from most forest fire studies, we included an urban area in our simulations. The downwind flow is further modified by the buildings in the residential area. The arrangement of the buildings has long been reported to change the flow regimes downwind (Oke, 1988). However, to the best of our knowledge, no previous study has investigated fire-atmosphere dynamics in a WUI with high fidelity. In addition to the complex surface flow in WUI, we also found that under certain fire weather, the wind shear at the upper level may impact fire-atmosphere interactions. The WUI has the potential to play a role in how the KH waves induced by the wind shear interact with the heat transport from the fire. To further understand the roles of WUI and the ambient atmosphere, a more detailed analysis is needed in the future. The spectral of the downwind heat transport from the fire should be analyzed, similarly to the turbulence spectra shown in e.g. Seto et al. (2013). To isolate the factors impacting fire-atmosphere interactions in the WUI, future work should include wavelet analysis (e.g. Desai et al., 2024), characterizing atmosphere turbulent structures and fire sweeps (Katurji et al., 2022), and spectral filtering of the wave signals (e.g. Kiladis et al., 2009).

It should be noted that high-fidelity simulations presented in this study are computationally expensive. A simulation of one hour presented here takes a wall clock time of 24 hours to finish on 900 Intel Skylake CPUs (running at 2.4 Ghz) distributed on the Cray XC50 platform. Moreover, this simulation is only one case study. To further understand the impact of WUI, one should conduct idealized simulations on, for example, the locations of the fire, the sizes of buildings and the gaps between the buildings, the size of the gap between wildland and urban areas, and so on. The design of the idealized studies should be careful, balancing the fidelity needed and the constraints on computation resources. Furthermore,

the simulations presented here only included heat forcing from fire, and no fire spread was simulated. The detailed fire behavior, such as combustion and fire flames, are not discussed. To include fire behavior with high-fidelity meteorological conditions and geospatial information, one of our future work centers around coupling PALM and WFDS. The coupled PALM-WFDS model would serve as a better tool to explore fire-atmospheric interactions.

5 Conclusions

In this study, we conducted high-fidelity simulations to investigate fire-atmosphere dynamics under a particular fire weather condition in the WUI of Bottle Lake Forest, Christchurch, New Zealand. Four simulations were conducted: WUI without fire (WUI_Base), WUI with fire (WUI_Fire), flat terrain without fire (Flat_Base), and flat terrain with fire (Flat_Fire). The fire heat forcing was obtained from field experiments. With the high-fidelity turbulence-resolving model PALM, we are able to investigate the three-dimensional fire-atmosphere interactions in great detail. To the best of our knowledge, no previous work has investigated fire-atmosphere interactions in WUIs with such a high resolution (finest at 4 m) in 3D. Comparing results between WUI and flat terrain simulations, we found that the presence of WUI brings huge modification and complexity to the flow structures. The fire heat footprints were illustrated for both WUI_Fire and Flat_Fire. The heat transfer from the prescribed fire reaches further downwind at all heights in WUI_Fire than that in Flat_Fire. The WUI landscape also causes a pulsing behavior of the downwind heat transport, which is absent in Flat_Fire.

To investigate the role of the WUI, the general flow characteristics were analyzed using violin plots. The WUI was split into three categories based on land use: forest, interface, and urban. Our results show that near the surface, the fire has little impact on the upwind flow but has a great impact on the downwind flow. Near the canopy height, the forest behind the fire experiences an increase in fire impact. On the downwind side, this increase is steeper over the interface and urban areas. The impact of the fire on the flows is intensified when WUI is present, especially in the increase in TKE. The analysis of the ambient atmosphere shows wave-like features induced by the KH waves. The differences between WUI_Base and Flat_Base are miniature, indicating that the WUI plays the main role in modifying fire-atmosphere interactions. Therefore, it is important to conduct high-resolution simulations with a realistic representation of the WUI environment for fire-atmosphere studies. Our results suggest that the presence of WUI could potentially worsen the fire spread and fire damage. Given that the WUI fire problem is escalating all over the world, results from this study could be helpful for future investigation of fire-atmosphere dynamics and fire management. Where to build the houses? How dense should the houses be? How do we design forest gaps? The high-fidelity simulations will be useful to answer these questions. Furthermore, high-fidelity simulations are important to understand ember transport. Ember transport is turbulent and has been identified as an important factor in fire danger management. These high-fidelity simulations can potentially provide more insights for future investigation of the fire-atmosphere turbulent flows.

This study mainly focuses on investigating the importance of the WUI environment in fire-atmosphere interactions. Although we documented several aspects of the WUI fire simulations, much work remains. Given the complexity of the simulations, the details of the dynamics are not explored. Future efforts will focus on explaining the causes of the heat pulsing and how WUI aids the transport of heat away from the fire. Future work also revolves around developing a coupled model of PALM and WFDS for better fire behavior modeling. The development of the coupled model will provide more insights into the role of WUI in fire-atmosphere interactions.

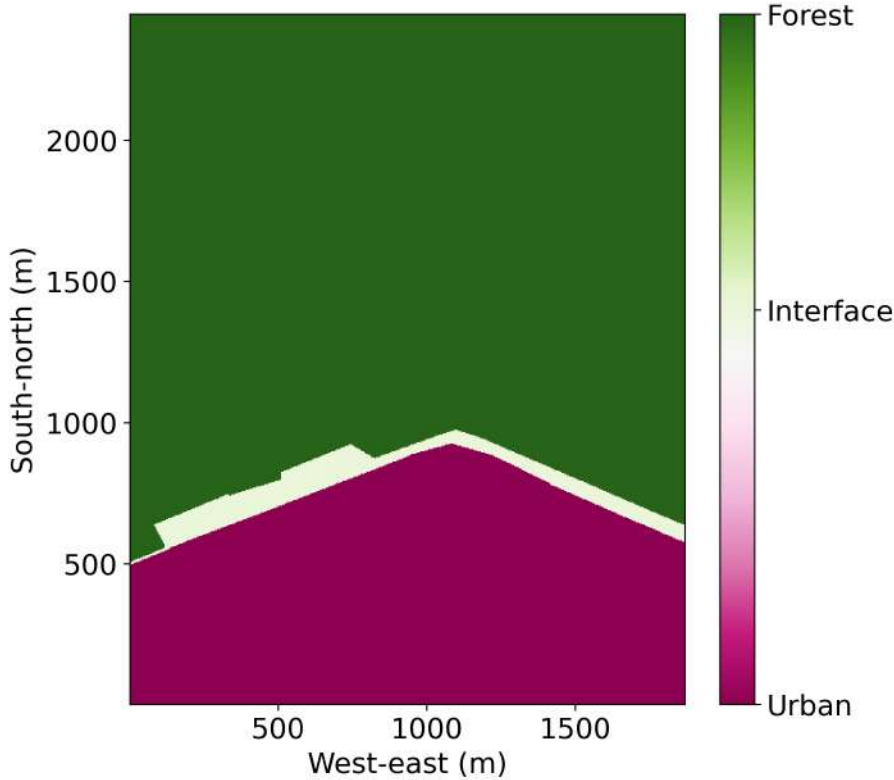


Figure A1. Land use classification for the violin plots shown in Figures 10 and 11.

Appendix A WUI land use classification

Open Research

We used the 22.10 release of the PALM model available from https://gitlab.palm-model.org/releases/palm_model_system/-/releases/v22.10 (last access: 10 June 2024). The modified version of PALM used in this study is available from (10.5281/zenodo.12798253; last access: 23 July 2024). The simulation output data can be shared upon request to the corresponding author.

Acknowledgments

This study was funded by the New Zealand Ministry of Business, Innovation and Employment (MBIE) project “Extreme wildfire: Our new reality – are we ready?” (Grant No. C04X2103). The New Zealand eScience Infrastructure (NeSI) high-performance computing facilities were used to conduct the simulations described in this paper. Simulation testing routines were done on the University of Canterbury high-performance research computing cluster (RCC) and the School of Earth and Environment (SEE) computing cluster.

References

- Andela, N., Morton, D. C., Giglio, L., Chen, Y., van der Werf, G. R., Kasibhatla, P. S., ... Randerson, J. T. (2017). A human-driven decline in global burned area. *Science*, 356(6345), 1356–1362. doi: 10.1126/science.aal4108
- Arakawa, A., & Lamb, V. R. (1977). Computational design of the basic dynamical processes of the ucla general circulation model. *General circulation models of the atmosphere*,

- 17(Supplement C), 173–265.
- Bakhshaii, A., & Johnson, E. (2019). A review of a new generation of wildfire–atmosphere modeling. *Canadian Journal of Forest Research*, 49(6), 565–574. doi: 10.1139/cjfr-2018-0138
- Belda, M., Resler, J., Geletič, J., Krč, P., Maronga, B., Sühling, M., ... Auvinen, M. (2021). Sensitivity analysis of the palm model system 6.0 in the urban environment. *Geoscientific Model Development*, 14(7), 4443–4464. doi: 10.5194/gmd-14-4443-2021
- Brody-Heine, S., Zhang, J., Katurji, M., Pearce, H. G., & Kittridge, M. (2023). Wind vector change and fire weather index in new zealand as a modified metric in evaluating fire danger. *International Journal of Wildland Fire*. Retrieved from <http://www.publish.csiro.au/?paper=WF22106> ([Online; accessed 2024-05-06]) doi: 10.1071/WF22106
- Chen, B., Wu, S., Jin, Y., Song, Y., Wu, C., Venevsky, S., ... Gong, P. (2024). Wildfire risk for global wildland–urban interface areas. *Nature Sustainability*, 1–11. doi: 10.1038/s41893-024-01291-0
- Clark, T. L., Coen, J., & Latham, D. (2004). Description of a coupled atmosphere–fire model. *International Journal of Wildland Fire*, 13(1), 49–63. doi: 10.1071/WF03043
- Clark, T. L., Jenkins, M. A., Coen, J., & Packham, D. (1996a). A coupled atmosphere fire model: Convective feedback on fire-line dynamics. *Journal of Applied Meteorology and Climatology*, 35(6), 875–901. doi: 10.1175/1520-0450(1996)035<0875:ACAMCF>2.0.CO;2
- Clark, T. L., Jenkins, M. A., Coen, J. L., & Packham, D. R. (1996b). A coupled atmosphere–fire model: Role of the convective froude number and dynamic fingering at the fireline. *International Journal of Wildland Fire*, 6(4), 177–190. doi: 10.1071/wf9960177
- Coen, J. (2013). Modeling wildland fires: A description of the coupled atmosphere–wildland fire environment model (cawfe). Retrieved from <https://opensky.ucar.edu/islandora/object/technotes%3A511/> doi: 10.5065/D6K64G2G
- Coen, J. L., Cameron, M., Michalakes, J., Patton, E. G., Riggan, P. J., & Yedinak, K. M. (2013). Wrf-fire: Coupled weather–wildland fire modeling with the weather research and forecasting model. *Journal of Applied Meteorology and Climatology*, 52(1), 16–38. doi: 10.1175/JAMC-D-12-023.1
- Dahl, N., Xue, H., Hu, X., & Xue, M. (2015). Coupled fire–atmosphere modeling of wildland fire spread using devs-fire and arps. *Natural Hazards*, 77(2), 1013–1035. doi: 10.1007/s11069-015-1640-y
- Dal-Ri dos Santos, I., & Yaghoobian, N. (2023). Effects of urban boundary layer turbulence on firebrand transport. *Fire Safety Journal*, 135, 103726. doi: 10.1016/j.firesaf.2022.103726
- Deardorff, J. W. (1980). Stratocumulus-capped mixed layers derived from a three-dimensional model. *Boundary-Layer Meteorology*, 18(4), 495–527. doi: 10.1007/BF00119502
- Desai, A., Guilloteau, C., Heilman, W. E., Charney, J. J., Skowronski, N. S., Clark, K. L., ... Banerjee, T. (2024). Investigating fire–atmosphere interaction in a forest canopy using wavelets. *Boundary-Layer Meteorology*, 190(5), 21.
- Dickinson, M. B., Wold, C. E., Butler, B. W., Kremens, R. L., Jimenez, D., Sopko, P., & O’Brien, J. J. (2021). The wildland fire heat budget—using bi-directional probes to measure sensible heat flux and energy in surface fires. *Sensors*, 21(6), 2135. doi: 10.3390/s21062135
- Dong, W., Fritts, D. C., Liu, A. Z., Lund, T. S., & Liu, H.-L. (2023). Gravity waves emitted from kelvin-helmholtz instabilities. *Geophysical Research Letters*, 50(8), e2022GL102674.
- Environment Canterbury Regional Council. (2020). *Christchurch and ashley river, canterbury, new zealand 2018*. doi: <https://doi.org/10.5069/G91J97WQ>
- Filippi, J.-B., Bosseur, F., Pialat, X., Santoni, P.-A., Strada, S., & Mari, C. (2011). Simulation of coupled fire/atmosphere interaction with the mesonh-forefire models. *Journal of Combustion*, 2011, e540390. doi: 10.1155/2011/540390
- Filippi, J.-B., Pialat, X., & Clements, C. B. (2013). Assessment of forefire/meso-nh for

- wildland fire/atmosphere coupled simulation of the fireflux experiment. *Proceedings of the Combustion Institute*, 34(2), 2633–2640. doi: 10.1016/j.proci.2012.07.022
- Finney, M. A., Cohen, J. D., Forthofer, J. M., McAllister, S. S., Gollner, M. J., Gorham, D. J., ... English, J. D. (2015). Role of buoyant flame dynamics in wildfire spread. *Proceedings of the National Academy of Sciences*, 112(32), 9833–9838. doi: 10.1073/pnas.1504498112
- Fire Emergency New Zealand. (2021). *New zealand wildfire summary 2020/21 wildfire season update*. ([Online; accessed 2024-06-21]) doi: <https://www.fireandemergency.nz/assets/Documents/Research-and-reports/NZ-Wildfire-2020-21-Season-update-Scion.pdf>
- Fire Emergency New Zealand. (2022). *Lake Ōhau wildfire investigation report and operational review*. ([Online; accessed 2024-06-21]) doi: <https://www.fireandemergency.nz/research-and-reports/operational-reviews-and-reports/lake-ohau-wildfire-investigation-report-and-operational-review/>
- fireFoam dev. (2023). *firefoam-dev/firefoam-v1912*. Retrieved from <https://github.com/fireFoam-dev/fireFoam-v1912> (original-date: 2022-04-07T05:43:57Z)
- Gehrke, K. F., Sühling, M., & Maronga, B. (2021). Modeling of land–surface interactions in the palm model system 6.0: land surface model description, first evaluation, and sensitivity to model parameters. *Geoscientific Model Development*, 14(8), 5307–5329. doi: 10.5194/gmd-14-5307-2021
- Gutierrez, A. A., Hantson, S., Langenbrunner, B., Chen, B., Jin, Y., Goulden, M. L., & Randerson, J. T. (2021). Wildfire response to changing daily temperature extremes in california’s sierra nevada. *Science Advances*, 7(47), eabe6417. doi: 10.1126/sciadv.abe6417
- Harlow, F. H., & Welch, J. E. (1965). Numerical calculation of time-dependent viscous incompressible flow of fluid with free surface. *The physics of fluids*, 8(12), 2182–2189.
- Heldens, W., Burmeister, C., Kanani-Sühling, F., Maronga, B., Pavlik, D., Sühling, M., ... Esch, T. (2020). Geospatial input data for the palm model system 6.0: model requirements, data sources, and processing. *Geosci. Model Dev. Discuss.*, 2020, 1–62. doi: 10.5194/gmd-2019-355
- Holden, Z. A., Swanson, A., Luce, C. H., Jolly, W. M., Maneta, M., Oyler, J. W., ... Affleck, D. (2018). Decreasing fire season precipitation increased recent western us forest wildfire activity. *Proceedings of the National Academy of Sciences*, 115(36), E8349–E8357. doi: 10.1073/pnas.1802316115
- Jiang, P., Wen, Z., Sha, W., & Chen, G. (2017). Interaction between turbulent flow and sea breeze front over urban-like coast in large-eddy simulation. *Journal of Geophysical Research: Atmospheres*, 122(10), 5298–5315.
- Kadasch, E., Sühling, M., Gronemeier, T., & Raasch, S. (2021). Mesoscale nesting interface of the palm model system 6.0. *Geoscientific Model Development*, 14(9), 5435–5465. doi: 10.5194/gmd-14-5435-2021
- Kanani-Sühling, F., & Raasch, S. (2017). Enhanced scalar concentrations and fluxes in the lee of forest patches: A large-eddy simulation study. *Boundary-Layer Meteorology*, 164(1), 1–17. doi: 10.1007/s10546-017-0239-0
- Katurji, M., Noonan, B., Zhang, J., Valencia, A., Shumacher, B., Kerr, J., ... Zawar-Reza, P. (2022). Atmospheric turbulent structures and fire sweeps during shrub fires and implications for flaming zone behaviour. *International Journal of Wildland Fire*, 32(1), 43–55. doi: 10.1071/WF22100
- Kiefer, M. T., Heilman, W. E., Zhong, S., Charney, J. J., & Bian, X. (2015). Mean and turbulent flow downstream of a low-intensity fire: Influence of canopy and background atmospheric conditions. *Journal of Applied Meteorology and Climatology*, 54(1), 42–57.
- Kiefer, M. T., Heilman, W. E., Zhong, S., Charney, J. J., & Bian, X. (2016). A study of the influence of forest gaps on fire–atmosphere interactions. *Atmospheric Chemistry and Physics*, 16(13), 8499–8509.
- Kiladis, G. N., Wheeler, M. C., Haertel, P. T., Straub, K. H., & Roundy, P. E. (2009).

- Convectively coupled equatorial waves. *Reviews of Geophysics*, 47(2).
- Krč, P., Resler, J., Sühling, M., Schubert, S., Salim, M. H., & Fuka, V. (2021). Radiative transfer model 3.0 integrated into the palm model system 6.0. *Geoscientific Model Development*, 14(5), 3095–3120. doi: 10.5194/gmd-14-3095-2021
- Kurppa, M., Roldin, P., Strömberg, J., Balling, A., Karttunen, S., Kuuluvainen, H., ... Timonen, H. (2020). Sensitivity of spatial aerosol particle distributions to the boundary conditions in the palm model system 6.0. *Geoscientific Model Development Discussions*, 1–33.
- Landcare Research. (2020). Lcdb v5.0 - land cover database version 5.0, mainland new zealand. ([Online; accessed 2020-07-15]) doi: <https://iris.scinfo.org.nz/layer/104400-lcdb-v50-land-cover-database-version-50-mainland-new-zealand/>
- Lin, D., Katurji, M., Revell, L. E., Khan, B., & Sturman, A. (2023). Investigating multiscale meteorological controls and impact of soil moisture heterogeneity on radiation fog in complex terrain using semi-idealised simulations. *Atmospheric Chemistry and Physics*, 23(22), 14451–14479. doi: 10.5194/acp-23-14451-2023
- Lin, D., Khan, B., Katurji, M., Bird, L., Faria, R., & Revell, L. E. (2021). Wrf4palm v1.0: a mesoscale dynamical driver for the microscale palm model system 6.0. *Geoscientific Model Development*, 14(5), 2503–2524. doi: 10.5194/gmd-14-2503-2021
- Lin, D., Zhang, J., Khan, B., Katurji, M., & Revell, L. E. (2024). Geo4palm v1.1: an open-source geospatial data processing toolkit for the palm model system. *Geoscientific Model Development*, 17(2), 815–845. doi: 10.5194/gmd-17-815-2024
- Linn, R., Reisner, J., Colman, J. J., & Winterkamp, J. (2002). Studying wildfire behavior using firetec. *International Journal of Wildland Fire*, 11(4), 233. doi: 10.1071/WF02007
- Mandel, J., Beezley, J. D., & Kochanski, A. K. (2011). Coupled atmosphere-wildland fire modeling with wrf 3.3 and sfire 2011. *Geoscientific Model Development*, 4(3), 591–610. doi: 10.5194/gmd-4-591-2011
- Maronga, B., Banzhaf, S., Burmeister, C., Esch, T., Forkel, R., Fröhlich, D., ... Russo, E. (2020). Overview of the palm model system 6.0. *Geoscientific Model Development*, 13, 1335–1372.
- Maronga, B., Gryschka, M., Heinze, R., Hoffmann, F., Kanani-Sühling, F., Keck, M., ... Raasch, S. (2015). The parallelized large-eddy simulation model (palm) version 4.0 for atmospheric and oceanic flows: model formulation, recent developments, and future perspectives. *Geoscientific Model Development*, 8(8), 2515–2551. doi: 10.5194/gmd-8-2515-2015
- Matvienko, O., Kasymov, D., Loboda, E., Lutsenko, A., & Daneyko, O. (2022). Modeling of wood surface ignition by wildland firebrands. *Fire*, 5(2), 38. doi: 10.3390/fire5020038
- Mell, W., Jenkins, M. A., Gould, J., & Cheney, P. (2007). A physics-based approach to modelling grassland fires. *International Journal of Wildland Fire*, 16(1), 1–22. doi: 10.1071/WF06002
- Mueller, S. E., Thode, A. E., Margolis, E. Q., Yocom, L. L., Young, J. D., & Iniguez, J. M. (2020). Climate relationships with increasing wildfire in the southwestern us from 1984 to 2015. *Forest Ecology and Management*, 460, 117861. doi: 10.1016/j.foreco.2019.117861
- Neves, T., Fisch, G., & Raasch, S. (2018). Local convection and turbulence in the amazonia using large eddy simulation model. *Atmosphere*, 9(10), 399. doi: 10.3390/atmos9100399
- Oke, T. R. (1988). Street design and urban canopy layer climate. *Energy and buildings*, 11(1-3), 103–113.
- Patton, E., & Coen, J. (2004). Wrf-fire: A coupled atmosphere-fire module for wrf [presentation]. Retrieved from <https://opensky.ucar.edu/islandora/object/conference%3A1315/>
- Pearce, H. (2018). The 2017 port hills wildfires-a window into new zealand's fire future? *Australasian Journal of Disaster and Trauma Studies*, 22, 35–50.

- Perry, G. L. W., Wilmschurst, J. M., & McGlone, M. S. (2014). Ecology and long-term history of fire in new zealand. *New Zealand Journal of Ecology*, 38(2), 157–176.
- Radeloff, V. C., Hammer, R. B., Stewart, S. I., Fried, J. S., Holcomb, S. S., & McKeefry, J. F. (2005). The wildland-urban interface in the united states. *Ecological Applications*, 15(3), 799–805.
- Resler, J., Krč, P., Belda, M., Juruš, P., Benešová, N., Lopata, J., . . . Kanani-Sühring, F. (2017). Palm-usm v1.0: A new urban surface model integrated into the palm large-eddy simulation model. *Geoscientific Model Development*, 10(10), 3635–3659. doi: 10.5194/gmd-10-3635-2017
- Salim, M. H., Schubert, S., Resler, J., Krč, P., Maronga, B., Kanani-Sühring, F., . . . Schneider, C. (2022). Importance of radiative transfer processes in urban climate models: a study based on the palm 6.0 model system. *Geoscientific Model Development*, 15(1), 145–171. doi: 10.5194/gmd-15-145-2022
- Serra-Neto, E. M., Martins, H. S., Dias-Júnior, C. Q., Santana, R. A., Brondani, D. V., Manzi, A. O., . . . Mortarini, L. (2021). Simulation of the scalar transport above and within the amazon forest canopy. *Atmosphere*, 12(12), 1631. doi: 10.3390/atmos12121631
- Seto, D., Clements, C. B., & Heilman, W. E. (2013). Turbulence spectra measured during fire front passage. *Agricultural and forest meteorology*, 169, 195–210.
- Sullivan, A., Baker, E., Kurvits, T., Popescu, A., Paulson, A. K., Cardinal Christianson, A., . . . Robinson, C. (2022). Spreading like wildfire: The rising threat of extraordinary landscape fires.
- Sullivan, A. L. (2009a). Wildland surface fire spread modelling, 1990 - 2007. 1: Physical and quasi-physical models. *International Journal of Wildland Fire*, 18(4), 349. doi: 10.1071/WF06143
- Sullivan, A. L. (2009b). Wildland surface fire spread modelling, 1990 - 2007. 2: Empirical and quasi-empirical models. *International Journal of Wildland Fire*, 18(4), 369. doi: 10.1071/WF06142
- Sullivan, A. L. (2017). Inside the inferno: Fundamental processes of wildland fire behaviour. *Current Forestry Reports*, 3(2), 150–171. doi: 10.1007/s40725-017-0058-z
- Sun, R., Krueger, S. K., Jenkins, M. A., Zulauf, M. A., & Charney, J. J. (2009). The importance of fire-atmosphere coupling and boundary-layer turbulence to wildfire spread. *International Journal of Wildland Fire*, 18(1), 50–60.
- Tang, T. (2017). A physics-based approach to modeling wildland fire spread through porous fuel beds. *Theses and Dissertations—Mechanical Engineering*. Retrieved from https://uknowledge.uky.edu/me_etds/84 doi: <https://doi.org/10.13023/ETD.2017.027>
- Trouvé, A., & Wang, Y. (2010). Large eddy simulation of compartment fires. *International Journal of Computational Fluid Dynamics*, 24(10), 449–466. doi: 10.1080/10618562.2010.541393
- Tse, S. D., & Fernandez-Pello, A. C. (1998). On the flight paths of metal particles and embers generated by power lines in high winds—a potential source of wildland fires. *Fire Safety Journal*, 30(4), 333–356. doi: 10.1016/S0379-7112(97)00050-7
- Valencia, A., Melnik, K. O., Kelly, R. J., Jerram, T. C., Wallace, H., Aguilar-Arguello, S., . . . Strand, T. (2023). Mapping fireline intensity and flame height of prescribed gorse wildland fires. *Fire Safety Journal*, 140, 103862. doi: 10.1016/j.firesaf.2023.103862
- Valencia, A., Melnik, K. O., Sanders, N., Hoy, A. S., Yan, M., Katurji, M., . . . Strand, T. (2023). Influence of fuel structure on gorse fire behaviour. *International Journal of Wildland Fire*, 32(6), 927–941. doi: 10.1071/WF22108
- Vogel, J., Afshari, A., Chockalingam, G., & Stadler, S. (2022). Evaluation of a novel wrf/palm-4u coupling scheme incorporating a roughness-corrected surface layer representation. *Urban Climate*, 46, 101311. doi: 10.1016/j.uclim.2022.101311
- Wang, Y., Chatterjee, P., & de Ris, J. L. (2011). Large eddy simulation of fire plumes. *Proceedings of the Combustion Institute*, 33(2), 2473–2480. doi: 10.1016/j.proci.2010.07.031

- 825 Wolf, T., Pettersson, L. H., & Esau, I. (2020). A very high-resolution assessment and
826 modelling of urban air quality. *Atmospheric Chemistry and Physics*, 20(2), 625–647.
827 doi: 10.5194/acp-20-625-2020
- 828 Zhang, J., Katurji, M., Brasington, J., Hilton, J., Zawar-Reza, P., & Strand, T. (2022).
829 Impact of forest gaps on wind turbulence and potential wildfire behavior at the rural-
830 urban interface. In *Advances in Forest Fire Research 2022* (pp. 615–625). Imprensa da
831 Universidade de Coimbra. Retrieved from [http://books.uc.pt/chapter?chapter=](http://books.uc.pt/chapter?chapter=978989262298994)
832 [978989262298994](http://books.uc.pt/chapter?chapter=978989262298994) doi: 10.14195/978-989-26-2298-9_94
- 833 Zhang, J., Katurji, M., Zawar-Reza, P., & Strand, T. (2023). The role of helicity and
834 fire-atmosphere turbulent energy transport in potential wildfire behaviour. *International Journal of Wildland Fire*, 32(1), 29–42. doi: 10.1071/WF22101
835